molecules

MDPI

Review

Recent Advances in g-C_3N_4-Based Materials and Their Application in Energy and Environmental Sustainability

Qian Wang [1,2,3], Yongfei Li [1], Fenglin Huang [1], Shaofu Song [1], Ganggang Ai [4], Xin Xin [5], Bin Zhao [6], Yajun Zheng [1] and Zhiping Zhang [1,*]

1 School of Chemistry and Chemical Engineering, Xi'an Shiyou University, Xi'an 710065, China
2 Xi'an Key Laboratory of Low-Carbon Utilization for High-Carbon Resources, Xi'an Shiyou University, Xi'an 710065, China
3 State Key Laboratory of Petroleum Pollution Control, Xi'an Shiyou University, Xi'an 710065, China
4 National Center for Quality Supervision and Inspection of Oil and Gas Products (Yan'an), Yan'an 716000, China
5 Department of Crop Soil Sciences, Washington State University, Pullman, WA 99164-6420, USA
6 Department of Statistics, North Dakota State University, Fargo, ND 58105, USA
* Correspondence: zhipingzhang@xsyu.edu.cn; Tel.: +86-29-8838-2694

Abstract: Graphitic carbon nitride (g-C_3N_4), with facile synthesis, unique structure, high stability, and low cost, has been the hotspot in the field of photocatalysis. However, the photocatalytic performance of g-C_3N_4 is still unsatisfactory due to insufficient capture of visible light, low surface area, poor electronic conductivity, and fast recombination of photogenerated electron-hole pairs. Thus, different modification strategies have been developed to improve its performance. In this review, the properties and preparation methods of g-C_3N_4 are systematically introduced, and various modification approaches, including morphology control, elemental doping, heterojunction construction, and modification with nanomaterials, are discussed. Moreover, photocatalytic applications in energy and environmental sustainability are summarized, such as hydrogen generation, CO_2 reduction, and degradation of contaminants in recent years. Finally, concluding remarks and perspectives on the challenges, and suggestions for exploiting g-C_3N_4-based photocatalysts are presented. This review will deepen the understanding of the state of the art of g-C_3N_4, including the fabrication, modification, and application in energy and environmental sustainability.

Keywords: g-C_3N_4; preparation; modification; hydrogen evolution; CO_2 conversion; organic pollutants

check for updates

Citation: Wang, Q.; Li, Y.; Huang, F.; Song, S.; Ai, G.; Xin, X.; Zhao, B.; Zheng, Y.; Zhang, Z. Recent Advances in g-C_3N_4-Based Materials and Their Application in Energy and Environmental Sustainability. *Molecules* **2023**, *28*, 432. https://doi.org/10.3390/molecules28010432

Academic Editor: Edgar Mosquera-Vargas

Received: 5 December 2022
Revised: 22 December 2022
Accepted: 25 December 2022
Published: 3 January 2023

1. Introduction

Along with the rapid growth of the global population and the development of industrialization and urbanization, the demand for fossil energy, such as petroleum, coal, and natural gas, is increasing, as well as the deterioration of environmental pollution [1]. Driven by the ongoing energy and ecological crisis, the development of sustainable energy is a matter of great urgency and is related to the vital interests of people worldwide. As a green and renewable energy, solar energy has become a hot topic [2] and converting it into chemical energy by using photocatalysis is regarded as a potential pathway to supply renewable energy and alleviate environmental issues in the future. The photocatalyst is the most important key in economic photocatalysis application; it should be efficient, stable, low-cost, and capable of harvesting visible light [3]. Many photocatalytic materials have been reported and used in various fields, including hydrogen evolution, contaminant photo-oxidization or photodecomposition, and photoelectrochemical conversion [4,5]. For example, titanium dioxide (TiO_2) and related photocatalysts have been used in solar energy conversion, due to their merits of low price, unique optical-electronic properties, great durability, and non-toxicity [6]. However, the large bandgap of TiO_2 (3.2 eV) prevents it from actual solar energy utilization [7,8]. Compared to TiO_2, the newly emerged graphitic carbon

nitride (g-C_3N_4) is a visible-light-response material with a narrower bandgap of 2.7 eV. It is a kind of metal-free photocatalyst and possesses the advantages of simple synthesis, suitable semi-conducting properties, and high structural stability under both thermal and photochemical conditions. These merits make g-C_3N_4 a unique material for energy and environmental applications, including photocatalytic H_2 generation, CO_2 reduction, and degradation of organic pollutants (dyes, pesticides, pharmaceuticals, phenolic compounds) and inorganic pollutants like heavy metals, carbon dioxide reduction, etc. [6,9–14]. In 2009, Wang et al. [15] for the first time proved that g-C_3N_4 could be used for photocatalytic hydrogen production upon visible-light irradiation, marking a significant milestone in metal-free photocatalysts. Nevertheless, due to the rapid recombination of photo-induced charges, the photocatalytic performance of g-C_3N_4 still possesses a significant possibility to be further enhanced, and the research on g-C_3N_4 gives rise to a new upsurge. So far, different strategies have been adopted to increase the photocatalytic efficiency of g-C_3N_4, such as morphological control, element doping, heterojunction construction, and nanomaterial composition [8,16,17]. In this review, we introduce the recent advances in the preparation and modification of g-C_3N_4, and summarize its photocatalytic application in H_2 generation, CO_2 reduction, and degradation of organic pollutants in recent years. Finally, we conclude the research challenges with g-C_3N_4 and suggest perspectives for future research direction.

2. Properties and Preparation of g-C_3N_4

2.1. The Origin and Properties of g-C_3N_4

Carbon nitride (C_3N_4), composed of carbon and nitrogen elements, is a kind of organic semiconductor material. The history of C_3N_4 can be traced back to 1834. One type of material named "melon" was synthesized by Berzelius and also reported by Liebig, which is a linear polymer connected triazine and tri-s-triazines (Figure 1) via secondary nitrogen [18,19]. However, this material did not attract much attention due to the lack of comprehensive characterization at the time. Along with the development of characterization methods, Franklin [20] probed this material in 1922 and proposed the concept of C_3N_4, which indicated that C_3N_4 could be obtained by polymerizing various ammonia carbonic acids. Later, Pauling and Sturdivant [21] demonstrated that tri-s-triazine was the unit of melon in 1937. Still, its chemical instability and insolubility in most reagents made it impossible to unveil the structure until 1989, researchers found that when Si in β-Si_3N_4 was replaced by C, the derived β-C_3N_4 was as hard as a diamond [22]. Based on the study, five types of C_3N_4, comprising α, β, pseudocubic, cubic, and graphitic, were predicated in 1996 [23]. Among them, the first four materials are hard materials but not favorable to be synthesized due to their low stability [24] and g-C_3N_4 is confirmed as the most resistant under surrounding situations; it possesses a similar layered structure to graphene and sp2 hybrid π-conjugated electronic band structure. In recent years, large numbers of g-C_3N_4 materials have been synthesized by thermal polymerization of urea, melamine, cyanamide, dicyandiamide, and thiourea, which indicated that g-C_3N_4 was composed of melem units and further confirmed that tri-s-triazine was the basic unit of g-C_3N_4.

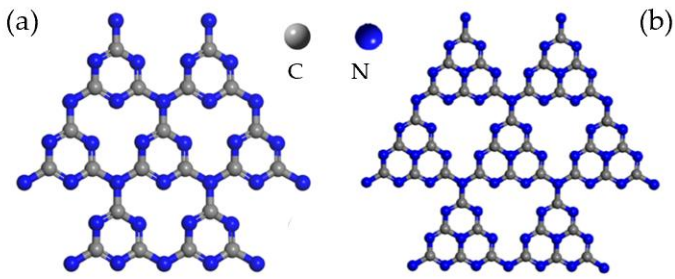

Figure 1. Structures of (**a**) triazine and (**b**) tri-s-triazine. Reprinted with permission from Ref. [25]. Copyright 2021 American Chemical Society.

The electronic structures of both carbon and nitrogen atoms in g-C_3N_4 determine their electronic and optical properties. The lone pair electrons of carbon and nitrogen atoms of g-C_3N_4 interact to create a large π bond, analogous to the benzene ring, and then form a highly delocalized conjugate system. The delocalized conjugate chemical structure contributes to the formation of the stacking of the carbon nitride layer, which connects through amines, and such a structure makes the superior electronic conductivity of g-C_3N_4 [1]. In addition, the solid covalent bond between carbon and nitrogen atoms leads to the excellent chemical and thermal stability of g-C_3N_4. After experimental measurements [26,27] the conduction band (CB) and valence band (VB) of g-C_3N_4 are −1.3 V and 1.4 V at pH = 7 versus the standard hydrogen electrode (SHE), respectively. Such band positions promote visible light harvesting under oxidation and reduction systems. In short, g-C_3N_4 possesses unique electronic, structural, physicochemical, and optical properties, sufficient for photocatalytic application in H_2 production, CO_2 photoreduction, and degradation of organic pollutants [9,28].

2.2. Preparation of g-C_3N_4

The property of a catalyst varies substantially depending upon the preparation protocols. To achieve the application of g-C_3N_4 in the field of photocatalysis, the synthesis of high-performance g-C_3N_4 is a prerequisite. Various methods have been proposed, including thermal condensation, hydrothermal and solvothermal approaches, solid-state fabrication, self-hand synthesis, template-supported formation, deposition-precipitation, and ball milling process [1,29].

Among these methods, thermal condensation, a combination of polycondensation and polyaddition, is the most common method to prepare g-C_3N_4. Nitrogen-rich chemicals, such as melamine, urea, and dicyandiamide, are usually used as precursors, and after the deamination process, g-C_3N_4 is generated under high temperatures. For example, Yan et al. [30] synthesized g-C_3N_4 with a high photodegradation activity toward methyl orange in a semiclosed system with a two-step heat treatment. By investigating the influence of heating temperature upon the thermal condensation of melamine, the optimal reaction condition for g-C_3N_4 was 520 °C for 2 h. Liu et al. [31] used urea as a precursor and produced g-C_3N_4 on a large scale by pyrolysis under ambient pressure without additive assistance. The retainable pyrolysis-generated self-supporting atmosphere and the reaction temperature are two necessary conditions.

Hydrothermal synthesis is also one of the most widely used methods, which is beneficial to control the accuracy in influencing reaction molar ratio and physio-chemical properties [1]. Wu et al. [32] prepared oxygen-containing-groups-modified g-C_3N_4 (OG/g-C_3N_4) through an in situ one-step hydrothermal treatment of bulk g-C_3N_4 in pure water. Hydrothermal treatment at 180 °C could promote the increase in the specific surface area of the resulting product from 2.3 to 69.8 m^2 g^{-1}, and oxygen-containing groups (-OH and C=O) were also successfully grafted on the surface of OG/g-C_3N_4 via the interlayer delamination and intralayer depolymerization. Due to its high surface area and oxygen-containing surface properties, OG/g-C_3N_4 demonstrated high photocatalytic performance on H_2 evolution. Ahmad et al. [33] synthesized a highly efficient double *Z*-scheme g-C_3N_4/AgI/β-$AgVO_3$ (g-CNAB) ternary nanocomposite using a one-pot hydrothermal route. They have characterized the optical properties, phase structure, and morphology of the as-prepared photocatalysts and evaluated their photocatalytic performance toward the photodegradation of different pollutants under visible-light irradiation. Experimental characterization indicated that g-CNAB possessed a dual *Z*-scheme heterojunction, which had the features of better spatial separation and charge-carrier transfer. As such, reactive species such as superoxide anion radical and hydroxyl radical can be favorably generated for the degradation of various contaminants.

To improve the photocatalytic performance of g-C_3N_4, templating strategy has also been applied to synthesize materials with unique appearance, structure, and properties. Due to the high specific surface area and low surface reflection, silica-based materials,

including silica spheres, mesoporous silica, and SBA-15, usually serve as hard templates to fabricate g-C_3N_4. Sun et al. [34] used silica as a template to prepare a highly stable, hollow g-C_3N_4 nanosphere (HCNS) (Figure 2). Adjustable shell thickness performed as a light-harvesting platform for H_2 evolution under visible light irradiation. However, corrosive reagents (e.g., NaOH, NH_4HF_2) are often used to remove silica templates, which are not friendly to the environment. On the contrary, the soft templating method uses ionic liquid as a template or co-template to fabricate g-C_3N_4, which is an environmentally friendly and one-step approach to prepare g-C_3N_4 with excellent performance. Zhao et al. [35] utilized cyanuric acid-melamine complex and an ionic liquid as soft templates to prepare hollow g-C_3N_4 spheres with a specific surface area as high as 84 m^2 g^{-1}. The morphology of g-C_3N_4 could be well controlled by adjusting ionic liquid and solvent. It has been demonstrated that the as-prepared hollow mesoporous carbon nitride exhibits ~30 times higher than traditional g-C_3N_4 in hydrogen production. Although significant progress has been achieved in the preparation and modification of g-C_3N_4, some preparation methods are neither environmentally friendly nor time-saving. Thus, it is necessary to develop green and facile synthesis routes.

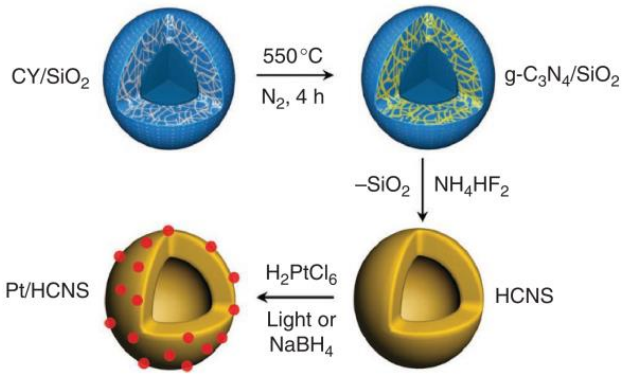

Figure 2. Illustration of HCNS and metal/HCNS composite syntheses. Reprinted with permission from Ref. [34]. Copyright 2012 Nature Publishing Group.

3. Modification of g-C_3N_4

3.1. Morphology Control

Morphology control of g-C_3N_4 is one of the practical and effective methods to improve its photocatalytic performance. g-C_3N_4 can be regulated to different dimensions (Figure 3). Then, with g-C_3N_4 having a larger specific surface area, more adequate active sites can be obtained. Moreover, the visible-light response range of g-C_3N_4 will be expanded, and the carrier diffusion path will be shortened. This section will discuss 0–3D g-C_3N_4-based materials and their catalytic performance.

3.1.1. 0D g-C_3N_4

g-C_3N_4 dots are new members of the g-C_3N_4 family, smaller than 10 nm in size, and have quantum size effect, surface effect, and quantum confinement effect [36]. As the size effect causes the reverse motion of CB and VB, g-C_3N_4 with broad absorption (from ultraviolet to visible light) can be obtained. The photogenerated charge carriers favorably migrate to the particle surface for initiating oxidation or reduction reactions. In recent years, a variety of low-cost and size-controlled methods have been developed to prepare g-C_3N_4 dots with different physicochemical properties, including hydrothermal treatment [37], ultrasonic exfoliation [38,39], microwave-assisted solvothermal process [40], and solid reaction approach [1]. A hydrothermal and hot-air assisted chemical oxidation method was proposed to prepare g-C_3N_4 QDs by etching bulk g-C_3N_4 to graphene-like nanosheets [41]. Concentrated H_2SO_4 and HNO_3 etched the nanosheets to produce g-C_3N_4 nanoribbons with sizes below 10 nm. Then, 5–9 nm g-C_3N_4 QDs can be obtained after the hydrothermal treatment of nanoribbons at 200 °C (pH = 5). The obtained g-C_3N_4 QDs

exhibited a strong blue emission and upconversion behavior, promising visible-light-driven metal-free photocatalytic systems. Liu et al. [38] synthesized g-C_3N_4 QDs by recrystallization and ultrasonic exfoliation from the precursor of dicyandiamide. g-C_3N_4 QDs with different sizes (5–200 nm) can be prepared by adjusting ultrasonic time up to 90 min. Chen et al. [40] prepared 0D/2D CNQDs/g-C_3N_4 isotype heterojunctions by a simple microwave assisted-polymerization method. The obtained product exhibited excellent photocatalytic performance toward norfloxacin degradation, and its reaction rate was as much as two times higher than pristine g-C_3N_4. Zero-dimensional QDs structure materials with nanometer size have a large surface/volume ratio, abundant surface atoms, and unsaturated coordination state, which conduce to their high activity for photocatalysis [42,43]. In addition, the absorption spectra of QDs/g-C_3N4 will appear blue shift, and band gaps will be broadened, affecting their electronic band structures in photocatalysis [44]. Thus, grafting 0D QDs on g-C_3N_4 is a promising approach to creating great reactive active sites and enhancing photoelectric conversion ability to improve photocatalytic activity.

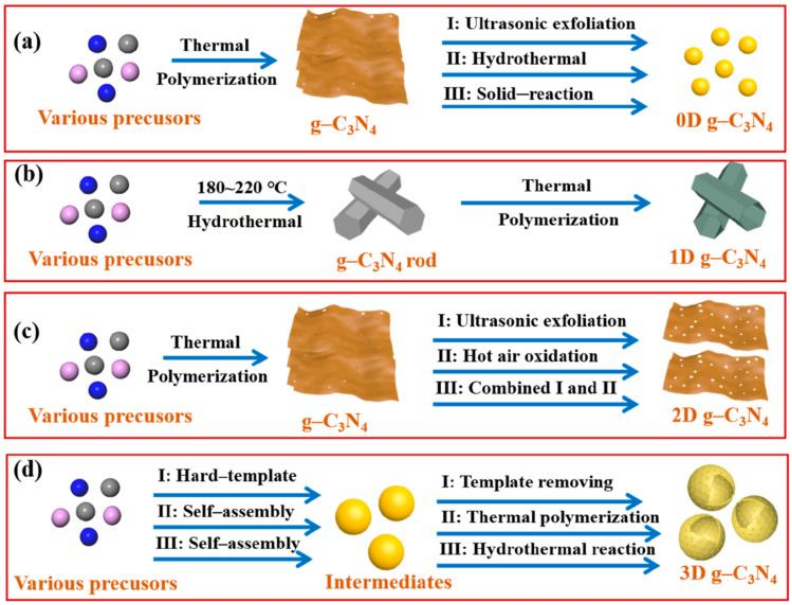

Figure 3. Schematic illustration of different techniques for the synthesis of (**a**) 0D g-C_3N_4, (**b**) 1D g-C_3N_4, (**c**) 2D g-C_3N_4, and (**d**) 3D g-C_3N_4. Reprinted with permission from Ref. [25]. Copyright 2021 American Chemical Society.

3.1.2. 1D g-C_3N_4

As morphology significantly affects materials' photochemical properties and electron transfer rate, the photocatalytic activity of g-C_3N_4 can be improved by adjusting its size and shape. The polymer characteristics of g-C_3N_4 make it an excellent flexible structure. One-dimensional g-C_3N_4, including nanowires [45], nanorods [46,47], and nanotubes [48], can be prepared by non-metallic hard-template, soft-template, self-template, and template-free methods. Bai et al. [47] found it possible to transform g-C_3N_4 from nanoplates to nanorods in a simple reflux way. They compared the photocatalytic activity and intensity of both shapes; results achieved in their study demonstrated that the photocatalytic activity and power of nanorods were ~1.5 and 2.0 times higher than those of nanoplates under visible light, attributable to an increase in active lattice face and elimination of surface defects. Jiang et al. prepared melamine crystals by a transitional metal derived re-crystalline process and then created g-C_3N_4 nanotubes with melamine crystals through a thermal polymerizing reaction method. They have applied transitional metal ions (Fe^{3+}, Co^{2+}, Ni^{2+}, and Mn^{2+}) in the growing of melamine crystals and have characterized the obtained ion-modified g-C_3N_4 nanotubes with XRD, FT-IR spectra, and XPS (Figure 4). It has been demonstrated that Fe^{3+}-ion-modified g-C_3N_4 nanotubes (Fe^{3+} R-650 CN) exhibited enhanced absorbance at 500 nm

and decreased band gap. The hydrogen evolution rate (7538 μmol h^{-1} g^{-1}) is almost 13.5-fold than that of conventional g-C_3N_4 nanosheets. Mo et al. [48] synthesized defect-engineered g-C_3N_4 nanotubes through an efficient self-assembled method, and applied them to hydrogen evolution. Around 6.8% external quantum efficiency was achieved at 420 nm. Among 1D g-C_3N_4, nanotubes are superior to others because they allow more effective light absorption, offer more active sites, and invent different electron pathways with tube morphology [25]. Generally, due to the nanometer scale of 1D g-C_3N_4-based materials in the radial direction, the diffusion distance (from volume to the surface) of photoexcited charges would be reduced, and the charge separation during photocatalytic reactions would be promoted. In addition, if g-C_3N_4-based materials are transformed from 2D to 1D structure, polygonal defects may appear to form the active sites and increase the contact surface of reactions, thus improving the photocatalytic performance.

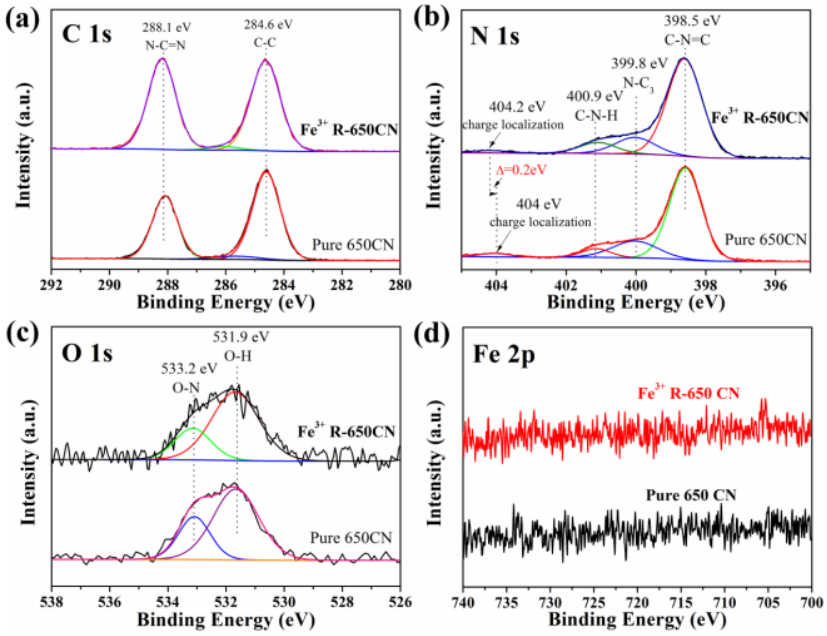

Figure 4. XPS spectra of samples pure 650 CN and Fe^{3+} R-650 CN. (**a**) C 1s. (**b**) N 1s. (**c**) O 1s. (**d**) Fe 2p. Reprinted with permission from Ref. [49]. Copyright 2019 John Wiley and Sons.

3.1.3. 2D g-C_3N_4

Bulk g-C_3N_4, prepared by the traditional one-step calcination method, has a small specific surface area (10 m^2 g^{-1}), and the photogenerated electrons and holes tend to recombine, which reduces its photocatalytic activity [50]. Since g-C_3N_4 has a 2D layered structure connected by van der Waals force, it will produce unique chemical and physical properties as below when it is stripped into multilayer or single-layer nanosheets. First, the large surface area and easy access to active reaction centers facilitate interactions with reactants. Second, nanoscale thickness or even less can minimize the migration distance of charge carriers, ensuring the rapid transport of charge carriers from the bulk phase to the surface of a catalyst. As a result, it would effectively inhibit electron-hole pairs from recombination. Third, the unique two-dimensional flexible planar structure can enhance compatibility with various modification strategies, such as heterojunction construction, cocatalyst modification, and vacancy introduction. This feature further improves the quantum efficiency in a photocatalysis process [51]. Various methods have been developed to prepare g-C_3N_4 nanosheets, such as thermal oxidation etching, chemical peel etching, supramolecular self-assembly, and ultrasonic treatment of exudation [1,51]. Among these, thermal oxidation etching is the most common method, which can overcome van der Waals force between layers and peel bulk g-C_3N_4 into 2D nanosheets under high-temperature oxidation conditions. Niu et al. [52] prepared g-C_3N_4 nanosheets (~2 nm thickness) by thermal oxidation etching of bulk g-C_3N_4 in the air. UV-visible absorption (Figure 5A)

exhibits a blue shift of the intrinsic absorption edge in the nanosheets. Compared to the bulk (2.77 eV), the nanosheets possess a higher specific surface area and 0.2 eV larger bandgap (Figure 5B). These characteristics benefit electron transport along the in-plane direction and increase the lifetime of photoexcited charge carriers because of the quantum confinement effect. Furthermore, the average hydrogen evolution rate of nanosheets is 170.5 μmol h^{-1} under UV-visible light, which is 5.4 times higher than that of the bulk counterpart. Due to the simplicity of operation, the supramolecular self-assembly method has attracted much attention. For example, conventional melamine-cyanuric acid (MCA) complexes can be obtained by mixing melamine and cyanuric acid in a solution. However, the use of solvent limits the batch preparation of MCA complexes. To address this issue, Liu et al. [53] proposed synthesizing supramolecular precursors through hydrothermal treatment of dicyandiamide and prepared 3D holey g-C_3N_4 nanosheets with excellent photocatalytic performance. The precursor exhibited a similar structure to that of conventional MCA. In contrast, their thermal decomposition and morphology were different, which led to the distinction of microstructures, optical properties, charge recombination, photoelectrochemical behavior, and photocatalytic activity. The holey g-C_3N_4 can make up for the shortcomings of recombination of charge carriers, retarded visible light utilization, and the limited surface-active sites in the bulk g-C_3N_4 catalysts, which could contribute to their outstanding application in photocatalytic hydrogen evolution.

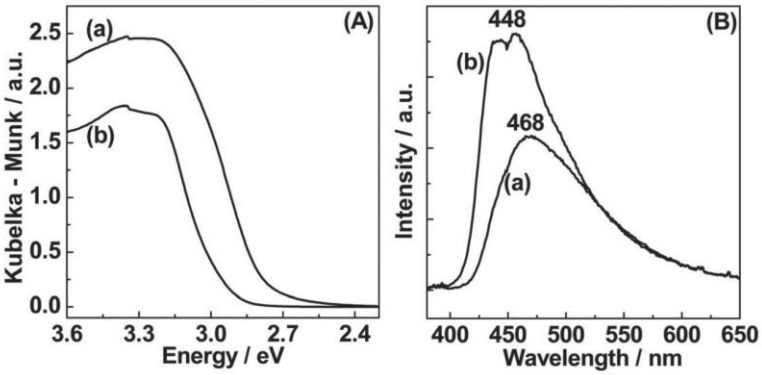

Figure 5. UV-visible absorption spectra (**A**) and fluorescence emission spectra (**B**) of: (a) bulk g-C_3N_4 and (b) g-C_3N_4 nanosheets. The wavelength of excitation light for fluorescence emission spectra is 350 nm. Reprinted with permission from Ref. [52]. Copyright 2012 John Wiley and Sons.

3.1.4. 3D g-C_3N_4

Three-dimensional nanostructures are considered an effective way to improve the properties of photocatalytic materials because they can provide a larger specific surface area and more reactive active sites. Although soft and hard template methods have been widely used in the preparation of 3D g-C_3N_4, they generally employ toxic substances and organic solvents to remove the template, which limits their application in actual green production. Salt templates have replaced some traditional templates (silica, sodium dodecyl sulfate, anodic alumina) for safe synthesis processes. Qian et al. [54] introduced a simple and effective sodium-chloride-assisted ball milling method to prepare 3D porous g-C_3N_4. Three-dimensional cubic sodium chloride particles can be used as an easily removable template to design 3D porous structures and as a limiting structure to prevent aggregation of g-C_3N_4 during calcination. The modified 3D interconnecting network structure of g-C_3N_4 has a large specific surface area, significantly improving the photocatalytic performance. The hydrogen production rate can be as high as 598 μmol g^{-1} h^{-1} with 3.31% quantum efficiency at 420 nm. In addition, ionic liquids are widely used in many fields due to their excellent fluidity and solubility. In the process of nanomaterial preparation, the ionic liquid can self-assemble into micelles, which impacts the size and morphology of the nanomaterials. For example, Zhao et al. [35] controlled the morphology of hollow mesoporous g-C_3N_4 spheres by changing ionic liquid concentration. At a low ionic liquid

concentration, the prepared mesoporous g-C_3N_4 showed a hollow spherical structure while, at a high ionic liquid concentration, the cyanate-melamine (CM) complex rearranged, which could induce the formation of a flower-like structure with ultrathin nanosheet (Figure 6). Moreover, the hollow as-prepared g-C_3N_4 exhibits higher light absorption in the visible range and a faster separation rate of photogenerated hole-electron pairs than bulk C_3N_4. In addition, the hydrogen production of as-prepared hollow mesoporous g-C_3N_4 exhibits ~30 times higher than traditional g-C_3N_4, because of its high surface area.

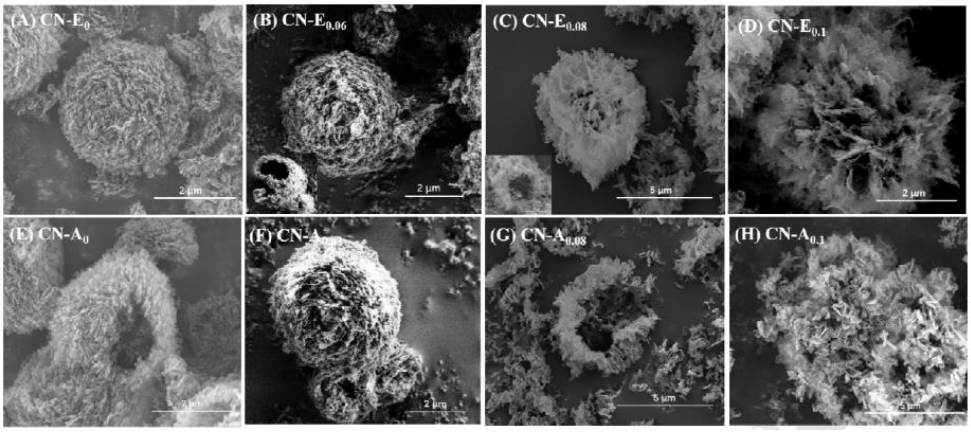

Figure 6. SEM images of hollow mesoporous carbon nitride spheres with different content of ionic liquid. Reprinted with permission from Ref. [35]. Copyright 2018 Elsevier.

In addition, some unique g-C_3N_4-based structures, like the "seaweed" network, spiral rod, and hollow fusiform, have also been reported [55–59], and a superior photocatalytic activity to bulk samples was observed for higher specific surface areas. Among these morphologies of g-C_3N_4, 1D nanoribbons, with a large specific surface area, more active sites, a short diffusion distance, and preferential directions for photo-generated electron-hole carriers, effectively accelerate the catalytic performance of g-C_3N_4. Better yet, the 3D morphology assembled from 1D units have depressed agglomeration, increased exposure of active sites, and decreased mass transportation resistance.

3.2. Elemental Doping

Heteroatom doping effectively regulates the electrical, optical, and structural properties of semiconductors by introducing active impurities [60]. In general, non-metallic heteroatoms can participate in the C_3N_4 lattice and partially replace C or N atoms, while metal atoms can insert into the triangular gap cavity of the g-C_3N_4 lattice. Doped metal and non-metal atoms generate intermediate band gaps near CB and VB to regulate the band structure of g-C_3N_4, which can effectively realize the separation and transmission of electron-hole pairs and broaden their optical response range [55,60]. Therefore, doping is a prevalent method to improve the photocatalytic performance of semiconductors.

3.2.1. Non-Metal Doping

Non-metal element doping could maintain the metal-free character of g-C_3N_4. Additionally, due to the high ionization energies and electronegativity of non-metals, they can quickly form covalent bonds with other compounds by gaining electrons during the reaction process [61,62]. The introduction of non-metals will break the symmetry of g-C_3N_4 and result in a faster separation speed of electron-hole pairs [63]. The ordinary non-metallic doping atoms include O, P, S, B, C, N, and halogens (F, Cl, Br, and I). Among them, the O atom, one of the most typical non-metallic doping elements, has shown extraordinary potential in improving the photocatalytic performance of g-C_3N_4. Zhang et al. [64] presented a hydrothermal method and fabricated a porous and oxygen-doped g-C_3N_4 photocatalyst for efficient photocatalytic hydrogen production by forming homogeneous supramolecular complexes (Figure 7). They introduced porous structure and heteroatom doping in

g-C_3N_4 to adjust its active sites and electronic structure for enhanced light harvesting, charge separation, and transfer. Compared with bulk g-C_3N_4, the hydrogen evolution activity of the g-C_3N_4 photocatalysts is 11.3-fold higher than bulk g-C_3N_4. She et al. [65] introduced oxygen in g-C_3N_4 and prepared 2D porous ultrathin oxygen-doped g-C_3N_4 nanosheets. It has been demonstrated that the band gap was enlarged (~0.20 eV), and the transport ability of photogenerated electrons and the redox ability were improved, which is caused by the quantum confinement effect. Besides, the specific surface area of non-metal doped g-C_3N_4 is larger (~20 times) than that of the bulk, which will supply more active sites with adequate quality and offer more adsorption sites. In short, due to the increased bandgap, the introduction of the electrophilic groups and the morphology structure, the electron-hole recombination probability is inhibited and the redox ability will be improved, which contribute to the enhanced photocatalytic activity.

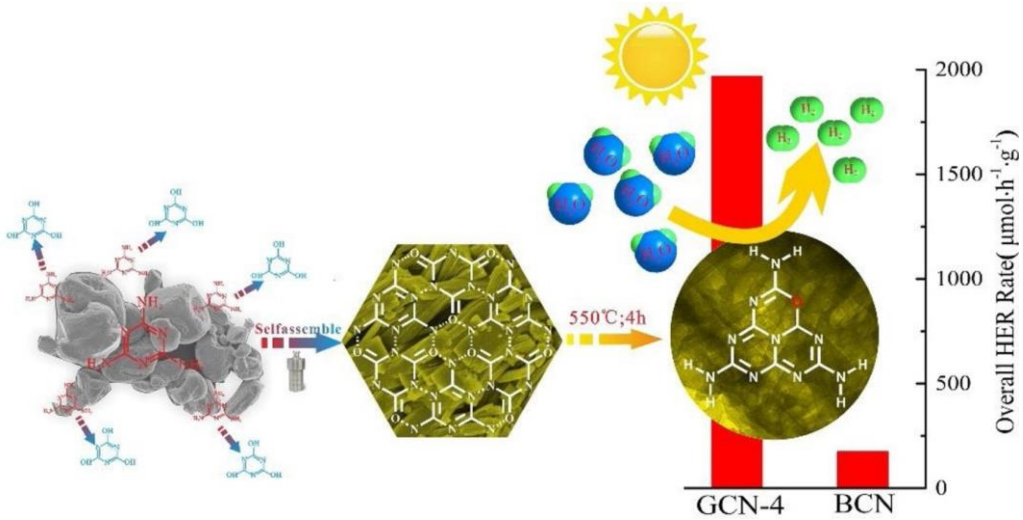

Figure 7. Illustration of the fabrication of porous *O*-doped g-C_3N_4 from hydrogen bond-induced supramolecular precursor assembled under hydrothermal treatment. Reprinted with permission from Ref. [64]. Copyright 2018 Elsevier.

3.2.2. Metal Doping

In terms of metal-doped g-C_3N_4, the porous structure of heptamine and electron-rich sp2 nitrogen atoms can provide sites for metal coordination, and doped metal can easily bind to the three neighboring N atoms in the form of g-C_3N_4. Metal element doping, especially alkali, has been demonstrated to reduce the energy gap, supply more active reaction sites, adjust VB position and improve photocarrier separation to enhance the visible light absorption [66]. Due to the uneven distribution of semiconductor charge space, the improvement of photogenerated carrier separation efficiency is increased. In addition, the alkali metal doping can increase the π-conjugated systems and reduce the recombination rate of the semiconductor electron-hole pairs, which will be beneficial to improve the efficiency of H_2 evolution by photolysis [67]. The ordinary doping metal atoms are K, Na, Ag, Au, Fe, Ni, Pt, etc. Gao et al. [68] designed a simple one-step pyrolysis process to synthesize Fe-doped g-C_3N_4 nanosheets with NH_4Cl as a "dynamic gas template" and $FeCl_3$ as a Fe source, respectively (Figure 8). The experimental results show that Fe species may exist at the state of Fe^{3+} and form Fe-N bonds in g-C_3N_4, thereby expanding visible light absorption regions and reducing the band gap of g-C_3N_4 nanosheets. Moreover, doping specific amounts of Fe could promote exfoliation and increase the specific surface area of g-C_3N_4, while excessive Fe might break the sheeting structure. The specific surface area of optimized Fe-doped g-C_3N_4 nanosheets reached 236.52 m^2 g^{-1}, which was 2.5 times higher than g-C_3N_4 nanosheets. In addition, Deng et al. [69] prepared K^+ and cyano-group co-doped crystalline polymeric carbon nitride (KC-CCN) by a one-step thermo-polymerization approach. They applied thiourea and potassium thiocyanate as

precursors, and the resulting KC-CCN demonstrated a highly crystal structure, stronger light harvesting, and a higher electron-hole separation ratio.

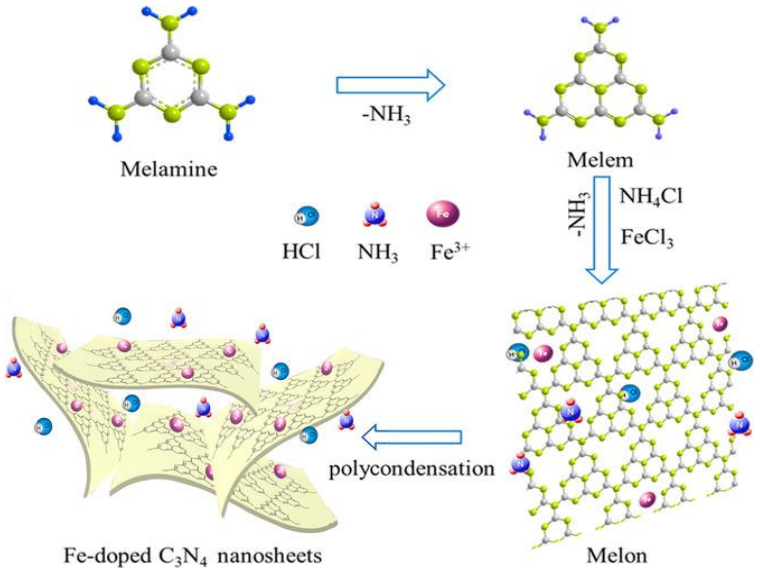

Figure 8. Schematic illustration of the synthesis process of Fe-doped g-C_3N_4 nanosheets. Reprinted with permission from Ref. [68]. Copyright 2017 John Wiley and Sons.

3.3. Heterojunction Construction

The key factor that restricts the activity of semiconductor photocatalysts is improving the separation and transport efficiency of electron-hole pairs. Thus, the construction of g-C_3N_4-based heterojunction photocatalysts is one of the most common and effective methods. When two semiconductors with different band structures combine to form a heterojunction, effective charge transfer will be included at the interface, improving charge separation and transport efficiency [70–74]. In addition, the light absorption capacity of a photocatalytic system can be enhanced by combining it with narrow-band gap semiconductors. For example, Xu et al. [75] proposed a wet chemical method to fabricate CdS/g-C_3N_4 (CSCN) heterojunctions in situ. Through the result of XRD, FTIR, TEM, and optical band gap for CSCN, the formation of heterojunctions was confirmed. The CdS nanoparticles dispersed uniformly on the surface of g-C_3N_4 nanosheets and the interfaces between g-C_3N_4 and CdS in composites is very close, which can efficiently enhance the electron transfer between the two semiconductors. Comparing the UV–vis DRS spectra of g-C_3N_4 (474.9 nm) and CdS (685.7 nm), the absorption thresholds of all CSCN composites locate between that of g-C_3N_4 and CdS, which indicates strong visible-light absorption. Among the materials, including the individual CdS, g-C_3N_4, and different CSCN composites, CSCN733 possesses the highest adsorption capacity and exhibits the highest methyl orange degradation efficiency, 100% with 40 min adsorption. Liu et al. [76] embedded nanorod-like CoP nanoparticles into g-C_3N_4 nanosheets to form CoP-CN heterostructure. The XRD data indicated that the 0.5% CoP-CN hybrid incorporates the representative peaks of g-C_3N_4 and CoP with g-C_3N_4 demonstrating the main phase. The TEM of 0.5% CoP-CN composites displays a porous and fluffy structure. The binding energy of P $2p_{3/2}$ is lower than that of P $2p_{3/2}$, while the binding energy of Co $2p_{3/2}$ eV is a little higher than that of metallic Co $2p_{3/2}$. This result indicates that the electron transfer from Co to P to form Co-P covalent bonds results in a small positive charge of Co and negative charge of P. This finding would account for the excellent activity of CoP-based photocatalysts in the HER process, in which Co serves as active center while P performs as the proton acceptor. The flat band potentials of 0.5% CoP-CN were decreased to −0.28 V and the CB tuned upward for more negative potential, achieving more efficient interfacial charge transportation and separation by establishing a certain inner electric field. Furthermore, among the

evaluation of photocatalytic water half-splitting for H_2 production, 0.5% CoP-CN exhibit excellent activity and reached 959.4 μmol h^{-1} g^{-1}, which is almost 3.1-fold than that of pristine g-C_3N_4 nanosheets. This can be attributed to its decreased over-potentials, more negative photo-reductive potentials, increased interfacial charge transfer efficiency, and higher solar-to-hydrogen efficiency. Ma et al. [77] combined TiO_2 with g-C_3N_4 to form a *Z*-type heterojunction, which can effectively separate photogenerated electrons and holes and improve the photocatalytic activity. However, the utilization of visible light of TiO_2 is very low because of its large band gap. Thus, to improve this weakness, the Eg of TiO_2 should be reduced, followed by its potential change of valence band and the conduction band. Such a move would change the heterojunction type, which is not consistent with improving the catalytic efficiency of composite materials to visible light. Therefore, various kinds of g-C_3N_4-based heterojunction photocatalysts have emerged to enhance the efficiency of photogenerated carrier separation further and light absorption capacity, including ternary [78–83] and other type II [84–88] and *S*-type heterojunction [89,90], Schottky junction [91,92], and van der Waals heterojunction [93,94].

The *S*-type heterojunction is composed of reduction photocatalysts (RPs) and oxidation photocatalysts (OPs) with staggered band structures, similar to the type-II heterojunction but with an entirely different charge-transfer route [95]. *S*-type photocatalysis is an effective way to control charge separation in various photocatalytic reactions. Since Yu et al. first proposed the concept of *S*-type heterojunction in 2019 [96], a large number of studies on the g-C_3N_4-based *S*-type heterojunction have been reported, such as Sb_2WO_6/g-C_3N_4 [97], *S*-doped g-C_3N_4/TiO_2 [98], $ZnFe_2O_4$/g-C_3N_4 [99], g-C_3N_4/$Zn_{0.2}Cd_{0.8}S$-DETA [100], g-C_3N_4/Bi/$BiVO_4$ [101], WO_3/g-C_3N_4 [102], etc. The Schottky junction photocatalyst has also attracted much attention. Generally, conductor-semiconductor heterojunction has two main combined modes: Schottky junction and ohmic contact. Conductors and semiconductors with different Fermi levels will generate Schottky effects at their contact interfaces to induce internal electric fields to drive charge flow until the system reaches equilibrium. The proper orientation of built-in electric fields will promote the directional separation of charge carriers, leading to the practical generation of photogenerated charge carriers and improving the photocatalytic activity. A large number of g-C_3N_4 Schottky junction photocatalysts have been reported, such as CoP/g-C_3N_4 [103], CuS/g-C_3N_4 [104], Ti_3C_2/g-C_3N_4 [105], carbon/g-C_3N_4 [106], MoO_2/g-C_3N_4 [107], Cu-NPs/g-C_3N_4 [108], etc. Recently, van der Waals (vdW) heterojunction has been proposed to regulate the electrical and optical properties of 2D materials accurately. vdW heterojunction not only overcomes the lattice matching limitation for enhancing interfacial charge separation and transfer but also leads to strong electronic coupling between layers to improve catalytic activity [109]. The research on g-C_3N_4-based vdW heterojunctions is currently enjoying a boom, and different types have been reported, including phosphorene/g-C_3N_4 [110], g-C_3N_4/Zn-Ti LDH [111], g-C_3N_4/C-doped BN [112], g-C_3N_4/COF package-TD [113], etc.

Moreover, metal-organic framework (MOF) materials have exhibited excellent photocatalytic performances due to their unique porous structures and favorable transfer of e^- and h^+ [114–116]. However, most MOFs have low stability and weak light response. Therefore, the heterojunction of MOF and g-C_3N_4 materials has become popular in recent years. For example, Zhang et al. [117] synthesized a novel hybrid of Zr-based metal-organic framework with g-C_3N_4 (UiO-66/g-C_3N_4) nanosheets (10:10) by annealing their mixture. The photoelectron can transfer efficiently from the CB of g-C_3N_4 to that of UiO-66 through the inner electric field generated by the heterojunction, which is beneficial to decrease the recombination of electron/hole. Together with their porous structures, much more organic dye molecules can absorb on the surface of the heterojunction catalyst, thus facilitating the electron/hole transfer and enhanced photocatalytic activity. Han et al. [114] prepared TPVT (tridentate ligand 2,4,6-tris(2-(pyridin-4-yl)vinyl)-1,3,5-triazine)-MOFs and combined them with g-C_3N_4. It has been demonstrated that the TPVT-MOFs@g-C_3N_4-10 can reach 56.4 μmol·g^{-1}·h^{-1} in CO_2 reduction, which is 3.2-fold higher than that of g-C_3N_4. All these

researches have provided a new insight into the design of g-C_3N_4 based photocatalysts to deal with the organic dyes in environment.

3.4. Modification with Carbon Nanocomposites

The weak van der Waals forces between layers and the abundant hydrogen bonds in the molecular structure make g-C_3N_4 exhibit slow charge transfer kinetics and poor electrical conductivity. Carbon materials have been widely used in photocatalysis due to their low price, good conductivity, high stability, non-toxicity, and harmlessness. Many composite photocatalysts with excellent photocatalytic performance have been prepared by combining carbon nanomaterials (such as fullerene [118], graphene [119], carbon nanotubes [120], etc.) with g-C_3N_4, which have unique nanostructures and excellent electron-optical properties (Figure 9). The introduction of carbon material reduces the electron-hole pair recombination rate of photocatalysts and improves the photo absorption, thus improving the photocatalytic performance of g-C_3N_4-based materials. g-C_3N_4 photocatalysts modified by carbon materials can promote photocatalytic reaction through heterojunction interaction, cocatalyst effect, surface recombination, local charge modification, and other ways [121]. For example, Yuan et al. [122] prepared a graphene-g-C_3N_4 composite photocatalyst by calcining graphene with melamine, and excellent photocatalytic degradation performance toward RhB was observed under acidic conditions. Ge et al. [123] prepared multi-walled carbon nanotubes (MWNTs)/g-C_3N_4 composite photocatalyst by heating MWNTs and g-C_3N_4, in which MWNTs favored the efficient separation of photo-generated charge carriers. As a result, this material exhibited unique performance in photocatalytic H_2 production under visible light conditions.

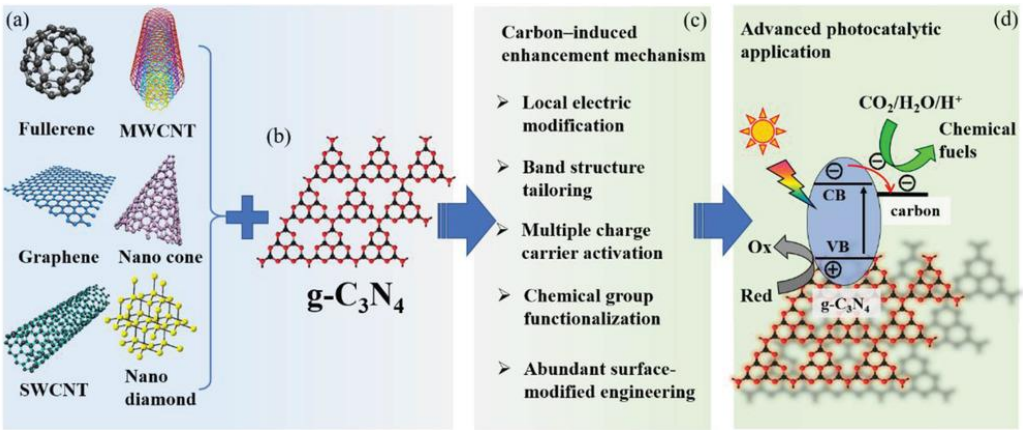

Figure 9. Schematic illustration of enhancement mechanism over carbon-induced g-C_3N_4 nanocomposites in photocatalytic action. (**a**) Different types of carbon materials. (**b**) Chemical structure of g-C_3N_4; black and red dots represent C and N, respectively. (**c**) The enhanced photocatalytic mechanisms and (**d**) energetic photocatalytic application of carbon-induced metal-free g-C_3N_4 nanocomposites. Reprinted with permission from Ref. [121]. Copyright 2020 John Wiley and Sons.

As a new carbon-based nanomaterial, carbon dots (CDs) exhibit excellent up-conversion photoluminescence and remarkable photogenerated charge-carrier transfer and reservoir [124–126]. They can also modify g-C_3N_4 and broaden optical absorption by reducing the electron-hole pair recombination rate [127,128]. Such features have caused extensive attention to CDs-modified g-C_3N_4. For instance, Fang et al. [129] prepared a CDs-modified g-C_3N_4 hybrid by dicyandiamide and CDs obtained from the combustion soot of alcohol. Based on the investigation of CDs modification on the structure and photocatalytic activity of g-C_3N_4, they found that CDs modification caused the lattice distortion of g-C_3N_4, and CDs performed as an electron sink, which could prevent the recombination of photo-generated electron-hole pairs. Ai et al. [130] reviewed the combination methods of g-C_3N_4 and CDs (Figure 10) for enhancing photocatalytic performance and indicated that

g-C_3N_4/CDs hybridization has strong practicability in efficient photocatalytic hydrogen generation, photocatalytic carbon dioxide reduction, and organic pollutant degradation. However, it is still in the early stage. Much effort should be made to develop green and facile synthesis routes and solve the insufficient utilization of visible and near-infrared light.

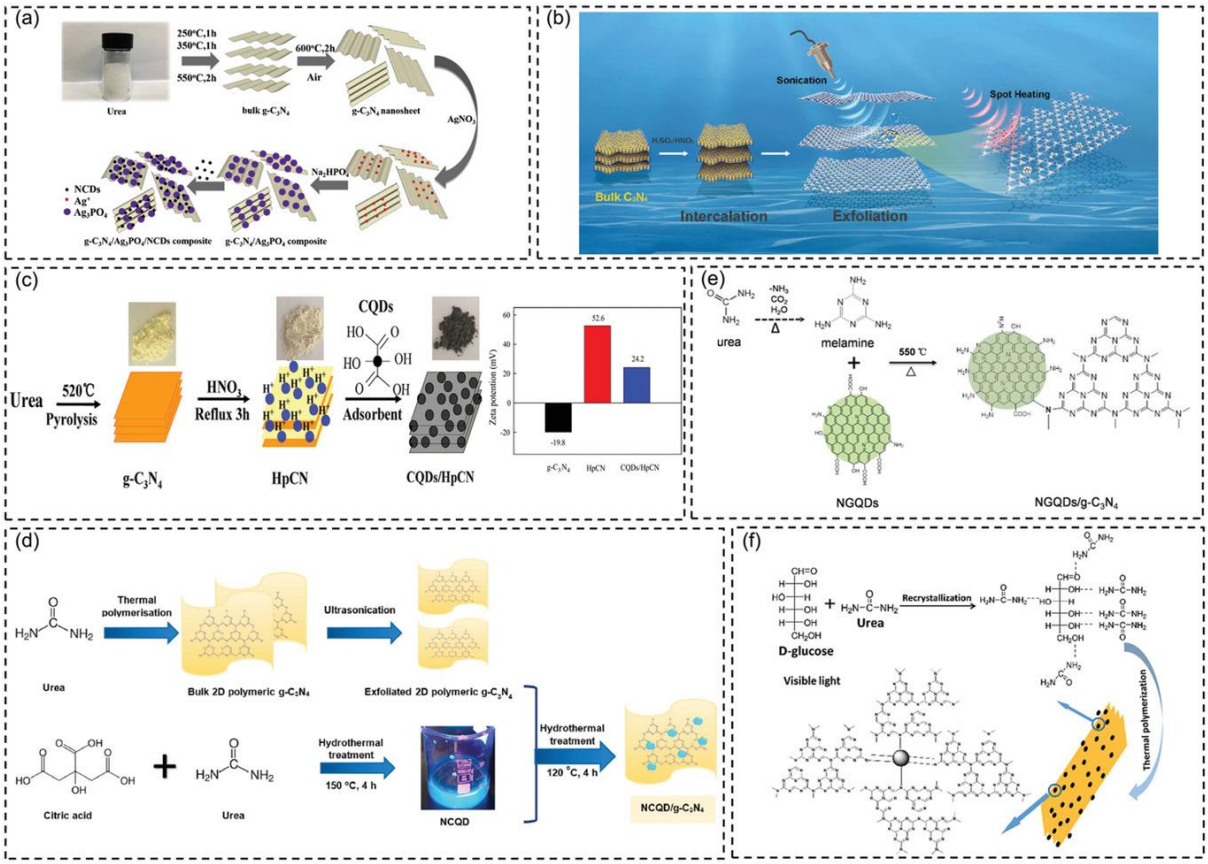

Figure 10. Schematic illustration of the preparation process for g-C_3N_4/CD-based nanocomposites through different methods. (**a**) Mechanical mixing method. (**b**) Ultrasonication method. (**c**) Electrostatic attraction method. (**d**) Hydrothermal/solvothermal method. (**e**,**f**) Calcine method. Reprinted with permission from Ref. [130]. Copyright 2021 John Wiley and Sons.

4. Photocatalytic Application in Energy and Environmental Sustainability

The energy and environmental crises have been an ongoing challenge, which is related to the vital interests of people around the globe. How to solve this problem through sustainable development strategies is considered deeply by scientific researchers. Photocatalysis provides a powerful technique for fully utilizing solar in the field of energy conversion [28,131]. Here, we will mainly introduce the photocatalytic application of g-C_3N_4 in energy and environmental remediation, including H_2 production, CO_2 photoreduction, and pollutant degradation.

4.1. H_2 Production

Hydrogen is gathering strong momentum as a pivotal energy transition pillar driven by the global shift toward decarbonization. Nevertheless, 85% of H_2 is produced from fossil fuel combustion, which generates roughly 500 metric tons of carbon dioxide every year and proffers a challenge and obstacle toward the sustainable living of future generations [132]. Solar-driven photocatalytic H_2 generation as a promising technology has received extensive attention in addressing the global energy crisis [133,134]. Photocatalytic water splitting for the energy transformation from solar to eco-friendly fuels has been studied for decades with various semiconductor photocatalysts. As a type of semicon-

ductor photocatalyst, g-C_3N_4 is simple and inexpensive to fabricate, and has an adequate bandgap (≈2.7 eV) for activation upon sunlight irradiation. Wang's group first utilized g-C_3N_4 in photocatalytic H_2 evolution [15,135]. Nonetheless, pristine g-C_3N_4 is far from satisfactory energy conversion because of its low light energy utilization, low density active sites, and ineffective isolation of the photogenerated excitons. Thus, researchers have proposed numerous strategies to boost the photocatalytic activity of g-C_3N_4-based materials for H_2 production. For example, the g-C_3N_4/carbon-dot-based nanocomposites, which possess enormous visible light absorption and applicable energy structures, have been prepared and serve as efficacious photocatalysts in photocatalytic water splitting for H_2 generation under light illumination [128,134,136,137]. Gao et al. reported hexagonal tubular g-C_3N_4/CD-based nanocomposites which exhibited nine times higher than bulk g-C_3N_4 in H_2 production rate [134] and related results indicated that CDs performed as both photosensitizer and electron acceptor. CDs could absorb long wavelength light to extend the visible-light response region and suppress the recombination of electron-hole pairs. Hussien et al. [138] combined four different strategies (non-metal doping, porosity generation, functionalization with amino groups, and thermal oxidation etching) in a one-pot thermal reaction and successfully prepared amino-functionalized ultrathin nanoporous B-doped g-C_3N_4 by using NH_4Cl as a gas bubble template, together with a thermal exfoliation process to produce ultrathin sheets (Figure 11). According to the process, the surface area, adsorption capacity, and charge migration of the as-prepared photocatalyst have been improved, and a 3800 μmol g^{-1} h^{-1} H_2 generation rate and 10.6% prominent quantum yield were recorded. Li et al. [139] decorated carbon self-doping g-C_3N_4 nanosheets with gold-platinum (AuPt) nanocrystals through a photo-deposition route and compared the photocatalytic H_2 evolution performance of Pt/CCN, Au/CCN, Au/Pt/CCN, and Pt/Au/CCN, in which AuPt/CCN stood out and gave the highest H_2 generation rate (1135 μmol h^{-1}). The excellent performance can be ascribed to the non-plasmon-related synergistic effect of Au and Pt atoms in AuPt nanocrystals. Sun et al. [140] assessed the arrangements of metal- and non-metal-modified g-C_3N_4 composites in hydrogen evolution and found that the contribution of dye conjugation in non-metallic g-C_3N_4 composites favored their performance (Figure 12). However, the co-catalyst doping strategy was recommended for metallic g-C_3N_4 composites. In addition, the hybrid of MOF materials and g-C_3N_4 is also a good approach to develop novel photocatalysts. For example, Devarayapalli et al. [141] reported a g-C_3N_4/ZIF-67 nanocomposite and obtained a 2084 μmol g^{-1} H_2 production, which is 3.84-fold greater than that of bare g-C_3N_4.

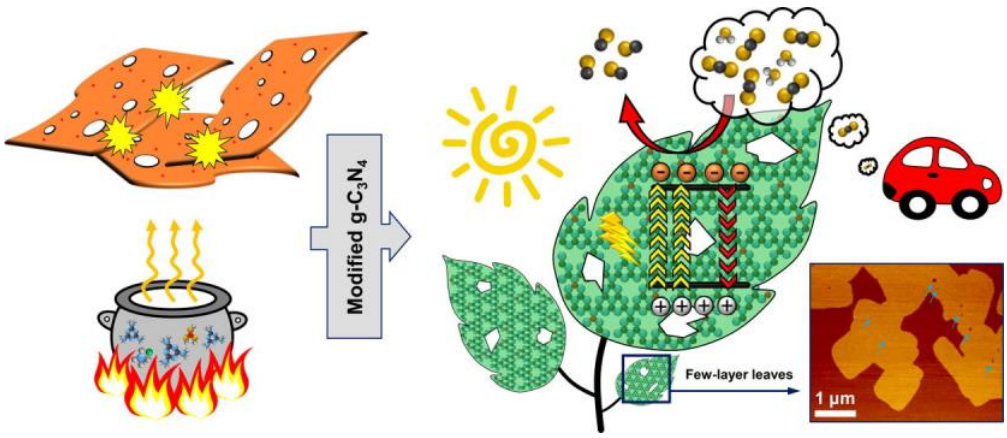

Figure 11. Scheme for a one-pot thermal preparation of amino-functionalized ultrathin nanoporous B-doped g-C_3N_4. Reprinted with permission from Ref. [138]. Copyright 2021 Elsevier.

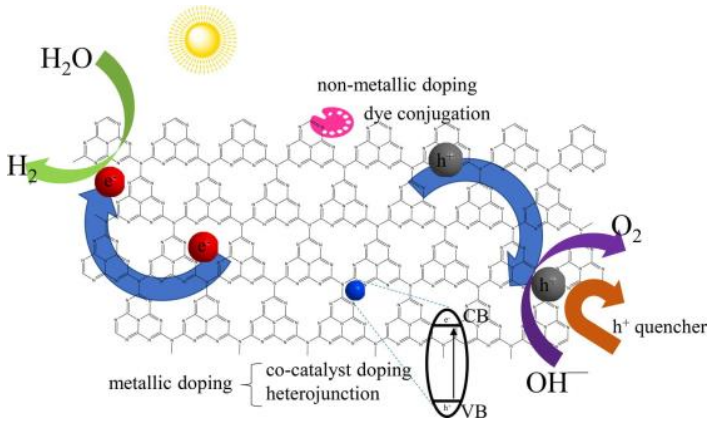

Figure 12. Schematic diagram for the performance comparison on hydrogen evolution between metal- and non-metal-modified g-C_3N_4 composites. Reprinted with permission from Ref. [140]. Copyright 2023 Elsevier.

Based on the descriptions mentioned above, Table 1 compares the performance of different g-C_3N_4-based materials for photocatalytic H_2 generation reported within the last three years.

Table 1. Photocatalytic H_2 generation over g-C_3N_4-based materials.

Entry	Photocatalyst	Experimental Details	H_2 Evolution Rate	Reference Material /μmol·g^{-1}·h^{-1}	Enhancement Relative to Conventional g-C_3N_4	Apparent Quantum Efficiency/%	Ref.
1	Cyano-group-modified crystalline g-C_3N_4 (CCN0.1)	50 mg CCN, 80 mL lactic acid (10 vol%), 1 wt% Pt/CCN	758.8 μmol·h^{-1}	Bulk g-C_3N_4 379.4 μmol·h^{-1}	2	1.17%	[142]
2	$Ba_5Nb_4O_{15}$/g-C_3N_4 (1:20)	420 nm LEDs (3 W single), Pt co-catalyst, 0.05 g, 100 mL oxalic acid	2.67 μmol·h^{-1}	g-C_3N_4 1.14 μmol·h^{-1}	2.35	6.1	[143]
3	P-doped g-C_3N_4 with aromatic ring (AS/P-CN)	300 W Xe, 10 vol% TEOA, 2 wt% Pt, 40 mg	550 μmol·h^{-1}·g^{-1}	Pristine CN 120 μmol·h^{-1}·g^{-1}	4.58	0.33	[144]
4	Ni_3S_2-NiS_2/CN-3	300 W Xe, 20 mg Ni_3S_2-NiS_2/CN-X, 90 mL water, 10 mL TEOA	1206.6 μmol·h^{-1}·g^{-1}	Pure g-C_3N_4 4.01 μmol·h^{-1}·g^{-1}	300.7		[145]
5	2% MoS_2-g-C_3N_4/Ni_2P	300 W Xe (>420 nm), 5 °C, 50 mg, 90 mL water, 10 mL of TEOA	298.1 μmol·h^{-1}·g^{-1}	Pure g-C_3N_4 4.32 μmol·h^{-1}·g^{-1}	69	2.51% (λ = 420 nm)	[146]
6	$HBTiO_2$/g-C3N4 QDs	300 W Xe, 0.025 g, 50 mL 0.25 M Na_2S, and 0.35M Na_2SO_3	10.57 mmol h^{-1}·g^{-1}	g-C_3N_4 0.32 mmol. h^{-1}·g^{-1}	33	18.6% 420 nm	[147]
7	0.8 wt.% g-C_3N_4/$BiVO_4$	200 mL lake water, 500 W halogen, 0.5 M Na_2SO_4	21.4 mmol h^{-1}			4.27% at 420 nm	[148]
8	g-C_3N_4/CoP-4%	350 W Xe, 10 mg, 70 mL water, 10 mL TEOA	936 μmol g^{-1} h^{-1}	g-C_3N_4—4 wt% Pt 665 μmol g^{-1} h^{-1}	1.41		[149]
9	NiCoP-3/C_3N_4	300 W Xe (300–780 nm), 100 mg, 10 mL methanol, 90 mL water	159 μmol g^{-1} h^{-1}	CoP-3/C_3N_4: 63.6 μmol g^{-1} h^{-1} Ni_2P-3/C_3N_4: 4.54 μmol g^{-1} h^{-1}	CoP-3/C_3N_4: 2.5 Ni_2P-3/C_3N_4: 35	4.2%	[150]
10	15% $FeSe_2$/CNNS 2D/2D composite	0.15/0.35 mol/L Na_2S/Na_2SO_3, 30 mg, 300 W Xe	1655.6 μmol g^{-1} h^{-1}	C_3N_4: 624.8 μmol g^{-1} h^{-1} $FeSe_2$: 957 μmol g^{-1} h^{-1}	Pristine g-C_3N_4: 2.65 $FeSe_2$: 1.73		[151]

Table 1. *Cont.*

Entry	Photocatalyst	Experimental Details	H_2 Evolution Rate	Reference Material /μmol·g^{-1}·h^{-1}	Enhancement Relative to Conventional g-C_3N_4	Apparent Quantum Efficiency/%	Ref.
11	5%-$NiCo_2O_4$/g-C_3N_4	300 W Xe, 50 mg, 100 mL solution (10 vol% of TEOA, 3% of H_2PtCl_6)	1041.9 μmol g^{-1} h^{-1}	g-C_3N_4 521.4 μmol g^{-1} h^{-1}	2		[152]
12	CoS/g-C_3N_4/NiS ternary photocatalyst	300 W Xe, 100 mg, 85 mL water, 15 mL TEOA	1.93 mmol h^{-1}·g^{-1}	Bare g-C_3N_4 0.15 mmol h^{-1}·g^{-1}	12.8	16.4% at 420 nm	[153]
13	5ZnO/ g-C_3N_4	0.2 g, 80 mL deionized water, 20 mL methanol	70 μmol h^{-1}	g-C_3N_4 8 μmol h^{-1}	8.75		[154]
14	20 wt% $CuFe_2O_4$/g-C_3N_4	200 W Hg−Xe, 20 mg, Na_2S/Na_2SO_3, TEOA	700.34 μmol g^{-1} h^{-1}	g-C_3N_4 nanosheets 280.1 μmol g^{-1} h^{-1}	2.5	25.09%	[155]
15	Boron-doped g-C_3N_4	150 W Xe, 20 mg, 10 vol% TEOA, Pt (1 wt%)	18.2 μmol h^{-1}	g-C_3N_4 6.1 μmol h^{-1}	3		[156]
16	3.0% β-Bi_2O_3/g-C_3N_4	500 W Xe, 50 mg, 200 mL glycerol (10% vol.)	8600 μmol g^{-1}	Bare β-Bi_2O_3 and g-C_3N_4 counterparts	>20		[157]
17	Pt/CN-A150 composite	300 W Xe, 10 mg, 100 mL DI water containing 20 vol% TEA	1150.8 μmol h^{-1}	Pt/CN-PR 18.2 μmol h^{-1} g-C_3N_4	63.2 4.6		[158]
18	g-C_3N_4@Ni_3Se_4 gC_3N_4@$CoSe_2$	5 W LED, 10 mg, 30 mL 15% *v/v* TEOA	16.4 μmol·h^{-1} 25.6 μmol·h^{-1}	Pristine g-C_3N_4 1.9 μmol·h^{-1}	8 13		[159]
19	MoS_2/g-C_3N_4	300 W Xe, 5 mg, 40 mL DI water, 10% *v/v* of TEOA	1787 mmol h^{-1} g^{-1}	MoS_2 g-C_3N_4	6 40		[160]
20	Carbon vacancies containing g-C_3N_4	300 W Xe, 100 mg, 90 mL deionized water, 10 mL TEOA, 3 wt% Pt	450 μmol h^{-1} g^{-1}	Pristine g-C_3N_4 225 μmol h^{-1} g^{-1}	2		[161]
21	3 wt% La_2NiO_4/g-C_3N_4	300 W Xe, 10 mg, 80 mL 20 vol% methanol	312.8 μmol h^{-1} g^{-1}	La_2NiO_4 5.8 μmol h^{-1} g^{-1} g-C_3N_4 7.1 μmol h^{-1} g^{-1}	53.8 43.9	3.7% 420 nm	[162]
22	18% Ag/AgBr/g-C_3N_4	300 W Xe, 50 mg, 90 mL deionized water, 10 mL TEOA	1587.6 μmol h^{-1} g^{-1}	g-C_3N_4 59.1 μmol h^{-1} g^{-1}	26.9		[163]
23	g-C_3N_4/N-doped carbon	300 W Xe, 10 mg, 20 mL 10 vol% TEOA, 0.5 wt% Pt	23.0 μmol h^{-1}	g-C_3N_4/C 5.9 μmol h^{-1}	4		[164]
24	Dendritic fibrous nanosilica/ g-C_3N_4-0.5	300 W Xe, 10 mg, 0.019 M, 80 μL K_2PtCl_4, 5 mL TEOA	4662 μmol h^{-1} g^{-1}	Pristine g-C_3N_4	7		[165]
25	$Ag_{0.1}Pd_{0.9}$/2D CNNs	300 W Xe, 100 mg, 3:1 FA/SF (1.0 M, 4 mL)	231.6 mmol h^{-1}	$Ag_{0.1}Pd_{0.9}$/2D CNNs under no light	1.87	27.8% 400 nm	[166]
26	g-C_3N_4/WO_3/WS_2	300 W Xe, 20 mg, 100 mL (20 vol%) TEOA	29 μmol h^{-1} g^{-1}	g-C_3N_4 nanosheets	7.8	8.9% 420 nm	[167]
27	CeO_2/g-C_3N_4-6	500 W Xe (400 nm), 0.1g, 100 mL 0.35 M Na_2SO_3 and 0.25 M Na_2S	1240.9 μmol h^{-1} g^{-1}	Pure CeO_2	5.2		[168]
28	Nitrogen vacancies-g-C_3N_4	3 W 420 nm LED, 0.02 g, 90 mL H_2O, 10 mL TEOA, 1% H_2PtCl_6 $2H_2O$ (10 mg/mL)	3259.1 μmol h^{-1} g^{-1}	Pristine g-C_3N_4	8.7		[169]
29	Black Cu-g-C_3N_4 nanosheets composite	300 W Xe, 10 mg 100 mL (1:9 TEOA: Water)	526 μmol h^{-1} g^{-1}	g-C_3N_4: 280			[170]
30	Amino-group-rich porous g-C_3N_4 nanosheets (AP-CN 1.0)	420-nm LED, 0.05 g, 80 mL 10 vol% TEOA, 1 wt% Pt	130.7 μmol h^{-1}	Bulk g-C_3N_4	4.9	5.58	[171]

Table 1. *Cont.*

Entry	Photocatalyst	Experimental Details	H_2 Evolution Rate	Reference Material /μmol·g^{-1}·h^{-1}	Enhancement Relative to Conventional g-C_3N_4	Apparent Quantum Efficiency/%	Ref.
31	0.3-MoS_2/g-C_3N_4	300 W Xe, 100 mg, 50 mL, deionized water and 5 mL TEOA	12 mmol h^{-1} g^{-1}	Pristine g-C_3N_4 g-C_3N_4 (Pt)	218 3	0.5% 420 nm	[172]
32	g-C3N4/ZIF-67	MaX 303 solar simulator, 20 mg, 0.5 M Na_2SO_4	2084 μmol g^{-1}	Bare g-C_3N_4 541 μmol g^{-1}	3.84		[141]
33	2D/2D ZnCoMOF/g-C3N4	300 W Xe, 10 mg, 0.1 mL DMF	1040.1		Bulk g-C_3N_4: 33.2 2D g-C_3N_4: 3.5		[116]
34	PCN-222(M)/g-C_3N_4	300 W Xe, 10 mg, 25 mL TEOA	1725.5 μmol h^{-1} g^{-1}		PNi: 19.3 CN: 3.7		[115]

4.2. CO_2 Photoreduction over g-C_3N_4

Rising atmospheric levels of CO_2 and the consumption of fossil fuels raise a concern about the continued reliance on the utilization of fossil fuels for both energy and chemical production [173]. Photocatalytic reduction of CO_2 is a promising strategy to meet increasing energy needs and reduce the greenhouse effect [174]. Through photocatalytic reduction, CO_2 can be converted to light oxygenates and hydrocarbons. Photocatalytic CO_2 reduction is a multielectron transfer process. Fu et al. [175] have listed the possible reaction and corresponding redox potentials and stated that CO_2 was complicated to reduce at room temperature due to its stable chemical structure. For the complex reaction, five factors, comprising the matching of band energy, separation of charge carrier, kinetic of e- and hole transfer to CO_2 and reductant, the basicity of photocatalyst, and the strength and coverage of CO_2 adsorption, are considered to be crucial [176]. As a hot member of photocatalysts, g-C_3N_4 has been applied to CO_2 photo-reduction in recent years because the CB of g-C_3N_4 is sufficient to reduce CO_2 to various hydrocarbons, such as CH_3OH, CH_4, HCHO, and HCOOH, etc. (Figure 13) [177].

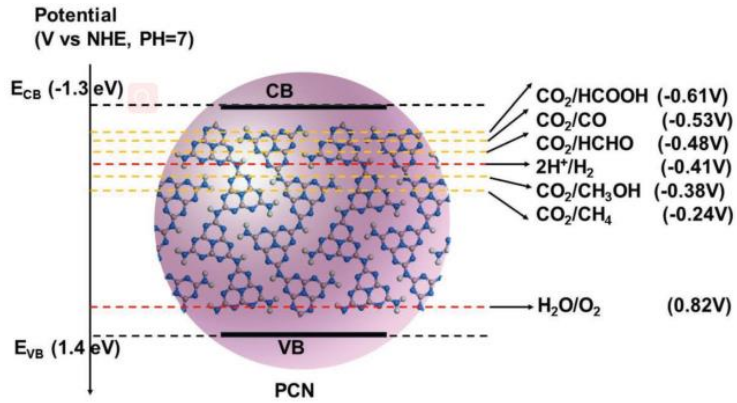

Figure 13. Schematic illustration of energy levels of PCN for photocatalytic CO_2 reduction. Reprinted with permission from Ref. [177]. Copyright 2019 John Wiley and Sons.

However, metal-free g-C_3N_4 is limited for CO_2 reduction activity due to its poor ability to activate the C-O bond of CO_2. To improve the photocatalytic movement of CO_2 conversion, different metal units have been composited with g-C_3N_4 for broadening the absorption response range, and accelerating the charge separation and transfer, such as Pt/g-C_3N_4 [178], Co^{2+}/g-C_3N_4 [179,180], Au/g-C_3N_4 [181], etc. Metal nanoparticles acting as cocatalysts could effectively improve the photocatalytic activity and selectivity of CO_2 reduction. In addition, other methods, including doping, loading cocatalysts and nanocarbons, constructing *Z*-scheme, and heterojunction, have also been employed [16,182–189]. For example, Fu et al. [190] prepared hierarchical porous *O*-doped g-C_3N_4 nanotubes (OCN-Tube) through continuing thermal oxidation exfoliation and curling condensation of

bulk g-C_3N_4. Due to the higher specific surface area, better light harvesting, higher CO_2 uptake capacity, and superior separation efficiency of photogenerated charge carriers, the OCN-Tube exhibits excellent photocatalytic CO_2 reduction performance into CH_3OH. The CH_3OH evolution rate was as high as 0.88 μmol g^{-1} h^{-1}, five times higher than the bulk (0.17 μmol g^{-1} h^{-1}). Huo et al. [191] fabricated amine-modified step-scheme (*S*-scheme) porous g-C_3N_4/CdSe-diethylenetriamine (A-PCN/CdSe-DETA) by a one-step microwave hydrothermal method. The modification by amine and formation of *S*-scheme heterojunction contributed to the remarkable photocatalytic performance of A-PCN/CdSe-DETA composite in CO_2 reduction and a CO production rate of 25.87 μmol/(h g) was achieved under visible-light irradiation. Wang et al. [174] reviewed different modification methods of g-C_3N_4-based photocatalysts for CO_2 reduction. They discussed each method (including morphology adjustment, co-catalysts, heterostructures, and doping) and compared the theoretical calculations and experimental results. By morphology adjustment, g-C_3N_4 with various shapes can be fabricated, such as rods, tubes, nanosheets, hollow spheres, and honeycomb-like structures. Due to the advantage of cocatalysts (e.g., Au, Ag, Pt, Pd, MXene, AuCu alloy, Pd-Ag), g-C_3N_4 with co-catalysts can be widely applied to activate CO_2 on the surface. Heterojunction with different types is also an effective method to improve the properties of g-C_3N_4-based materials. In addition, elemental doping is considered a common method to enhance photocatalytic quantum efficiency by changing the energy band, surface electronic property, and electrical conductivity. Table 2 compares the performance of different g-C_3N_4-based materials for photocatalytic CO_2 reduction reported within the last three years.

Table 2. Photocatalytic CO_2 reduction over g-C_3N_4-based materials.

Entry	Photocatalyst	Experimental Details	Productivity /μmol·g^{-1}·h^{-1}	Reference Material /μmol·g^{-1}·h^{-1}	Enhancement Relative to Conventional g-C_3N_4	Apparent Quantum Efficiency/%	Ref.
1	Ni/g-C_3N_4-0.5 catalyst	300 W Xe, 94–95 kPa, 10.0 mg, deionized water	CO: 19.9	g-C_3N_4: 4.8	4.1		[192]
2	*S*-scheme $CuWO_4$ @ g-C_3N_4 core-shell microspheres	300 W Xe (≥420 nm), 0.1 g $NaHCO_3$, 0.5 mL 4M HCl	CO: 4.15 CH4: 0.12	g-C_3N_4 CO: 1.56 CH_4: 0.02	2.7		[193]
3	Hydroxyl-modified g-C3N4/flower-like $Bi_2O_2CO_3$ composites	blue LED (4 × 3 W) 450 ± 20 nm, 40 mg, deionized water	CO: 26.69	Pristine g-C_3N_4 CO: 1.47	18.2		[194]
4	Z-scheme g-C3N_4/$BiVO_4$ (CN/BVO) heterojunction	300 W Xenon lamp, 0.05 g, 5 mL water	CO: 48	Pristine BVO CO: 2	24		[195]
5	Ultrathin dimension-matched *S*-scheme Bi_3NbO_7/g-C_3N_4 hetero-structure	Solar simulator, 50 mg, deionized water, 1.3 g Na_2CO_3, 2.0 mL H_2SO_4	CH_4: 37.59	Ultrathin g-C_3N_4 nanosheets CH_4: 2.5	15		[196]
6	Van der Waals (vdW) heterojunction composite combining g-C_3N_4 with nitrogen vacancies and Tp-Tta COF	300 W Xe, 20 mg, 15 mg bpy, 1 μmol $CoCl_2$, acetonitrile, water, TEOA	CO: 11.25	Pristine g-C_3N_4 CO: 0.25, g-C_3N_4 (NH) CO: 3.5	Pristine g-C_3N_4: 45 g-C_3N_4 (NH): 3.2		[197]
7	C-NHx-rich 24 g-C_3N_4	300 W Xe (420 nm), 10 mg g-C_3N_4, 10 mL deionized water, pH at 30 °C	CO: 185.7	g-C_3N_4 CO: 2.5	g-C_3N_4: 74		[198]
8	g-C_3N_4/3DOM-WO_3	300 W Xe (≥420), water, 0.1 g catalyst, 2 mL deionized water	CO: 48.7 CH4: 7.5 O2: 44.5	Pure g-C_3N_4 nanosheets CO: 25.2 CH_4: undetected	Pure g-C_3N_4 nanosheets CO: 1.9		[199]
9	g-C_3N_4/rGO composites	300 W Xe, 3 mg mL^{-1} catalysts, 5 mL 0.2 M $NaHCO_3$, illuminated 12 h	CH_3OH: 114	$CdIn_2S_4$/g-C_3N_4 CH_3OH: 42.7	$CdIn_2S_4$/g-C_3N_4: 2.67	0.63	[200]

Table 2. *Cont.*

Entry	Photocatalyst	Experimental Details	Productivity /μmol·g^{-1}·h^{-1}	Reference Material /μmol·g^{-1}·h^{-1}	Enhancement Relative to Conventional g-C_3N_4	Apparent Quantum Efficiency/%	Ref.
10	15% $LaCoO_3$ loaded g-C_3N_4	35 W Xe (420 nm), 50 mg photocatalyst, pressure 0.30 bar	CO: 135.2 CH_4: 48.5	Pristine La-CoO_3 CO: 110 CH_4: 28.5 g-C_3N_4 CO: 114 CH_4: 30.4	Pristine $LaCoO_3$ CO: 1.2 CH_4: 1.7 g-C_3N_4 CO: 1.18 CH_4: 1.59		[201]
11	$Bi_2O_2(NO_3)(OH)$/g-C_3N_4	300 W Xe, 20 mg samples, 3 mL DI water	CO: 14.84	BON CO: 0.94 g-C_3N_4 CO: 3.29	pure BON:15 g-C_3N_4: 3.5		[202]
12	Z-scheme SnS2/gC3N4/C	300 W Xe, 0.05 g catalyst 100 mL deionized water, 25 °C, 5 h	CO: 40.86	Pristine g-C_3N_4 CO: 7.42	Pristine g-C_3N_4 5.5		[203]
13	ND/g-C_3N_4	300 W Xe (>420 nm), 30 mg catalyst, 18 mL acetonitrile, 6 mL water, 1 μmoL $CoCl_2 \cdot 6H_2O$	CO: 10.98	CO: 0.59	bulk g-C_3N_4 18.6		[204]
14	$ZnIn_2S_4$ nanosheets modified hexagonal g-C_3N_4 tubes	300 W Xe (420 nm), 4 mg, 2 mL water, 1 mL of triethanolamine, 3 mL acetonitrile, 15 mg 2′2-bipyridine (bpy) and 2 μmol of $CoCl_2$	CO: 883	HCNT: 66 ZIS: 367.9	HCNT: 13 ZIS: 2.4	8.9%	[205]
15	g-C_3N_4/covalent triazine framework (CN/CTF 2.5%)	300 W Xe, 5 mg catalyst in 4 mL acetonitrile, 1 mL $Co(bpy)_3Cl_2$ triethanolamine	CO: 151.1	CTF: 5.93 CN: 60.44	CTF: 25.5 CN: 2.5		[206]
16	g-C_3N_4-$W_{18}O_{49}$ nanocomposite	300 W Xe, 50 mg catalyst in 1 mL deionized water	CH_4: 1.38	g-C_3N_4: 0.17 $W_{18}O_{49}$: 0.12	g-C_3N_4: 8.12 $W_{18}O_{49}$: 11.5		[207]
17	SnS_2/Au/g-C_3N_4 embedded structure	300 W Xe, 20 mg, 100 mL water and TEOA, 140 kPa	CO 93.81 CH_4 74.98				[208]
18	Bi_3O_4Cl/20%g-C_3N_4	300 W Xe, 0.05 g catalyst, 5 mL H_2O	CO: 6.6 CH_4: 1.9	Pure g-C_3N_4 CO: 2.2, CH_4: 0.6 Bi_3O_4Cl CO: 2.9 CH_4: 0.7	g-C_3N_4 CO: 3 CH_4: 3.17 Bi_3O_4Cl CO: 2.28 CH_4: 2.71	Bi_3O_4Cl/20% g-C_3N_4 is 0.14% under 365	[209]
19	2D/2D g-C_3N_4/$NaBiO_{32}H_2O$ (10 CN/NBO)	300 W Xe, 25 mg, deionized water, 1.2 g $NaHCO_3$, 2 mL H_2SO_4 (1:1 vol)	CO: 110.2 CH_4: 43.8	Pure CN CO: 65.68 CH_4: 0.42 NBO CO: 26.45 CH_4: 4.81	Pure CN CO: 1.68 CH_4: 104.3 NBO CO: 4.16 CH_4: 9.1		[210]
20	Ultrathin nanosheet g-C_3N_4 (NS-g-C_3N_4)	300 W Xe (420 nm), 0.1 g photocatalyst, 50 mL 50 g/L $KHCO_3$	CO: 38 μmol/L with 6 h	Bulk g-C_3N_4 CO: 6.56 μmol/L	CO: 5.8		[211]
21	3% CdS-g-C_3N_4 heterostructures	300 W Xe (420 nm), 1 g/L catalyst 100 mL H_2O, 80 °C, 125 mg Na_2CO_3, 0.25 mL HCl (4 M)	CH_3OH: 192.7	CdS CH_3OH: 47.1 pristine g-C_3N_4 CH_3OH: 32.6	CdS: 4.1 pristine g-C_3N_4: 5.9		[212]
22	Z-scheme ZnO/Au/g-C_3N_4 micro-needles film (3-ZAC)	300 W UV–vis lamp, fiberglass sheets, 0.4 M Pa	86.2 μmol m^{-2} h^{-1}	Pure ZnO 19.16 μmol m^{-2} h^{-1}	Pure ZnO film: 4.5		[213]
23	rGO/R-CeO_2/g-C_3N_4	300 W Xe, 100 mg catalysts, 100 mL 1 M NaOH, 1 mmol TEOA, 0.4 MPa	CO:15.8 CH_4: 8.15	CO: 3.95 CH_4: 1.36	Pure g-C_3N_4 CO: 4 CH_4: 6		[214]
24	g-C_3N_4/ZnO composites	300 W Xe (λ ≥ 420 nm), 60 mg catalysts, 1.60 g $NaHCO_3$, H_2SO_4 (40%, 5.0 mL)	CH_4: 19.8 CO: 0.37	g-C_3N_4 CH_4: 0.9 CO: 4.8	g-C_3N_4 CH_4: 22 CO: 0.078		[215]
25	K-CN-7	300 W Xe, 50 mg catalyst, 200 μL deionized water, 1 cm × 3 cm ITO glass; 0.5 M Na_2SO_4	CO: 8.7	Ordinary g-C_3N_4 CO: 0.348	Ordinary g-C_3N_4: 25		[216]

Table 2. *Cont.*

Entry	Photocatalyst	Experimental Details	Productivity /μmol·g^{-1}·h^{-1}	Reference Material /μmol·g^{-1}·h^{-1}	Enhancement Relative to Conventional g-C_3N_4	Apparent Quantum Efficiency/%	Ref.
26	g-C_3N_4/CdS heterostructure nanocomposite	150 W Xe, 20 mg catalyst, 7 mL acetone nitrile, 0.5 mL H_2O, 0.5 g TEOA, 4 μmol [Co(bpy)$_3$]Cl	CO: 234.6	CN-12: 58.65 CdS: 9.2	CN-12: 4.0 CdS: 25.5		[217]
27	Porous structure g-C_3N_4 with nitrogen defect photocatalysts (DCN-P)	300 W Xe, 0.05 g catalyst, 100 mL deionized water	CO, 19.7 CH_4: 37.1	Bulk g-C_3N_4 CO: 4.1 CH4: 9.6	Bulk gC_3N_4 CO: 4.8 CH_4: 3.86		[218]
28	g-C_3N_4/Bi_2O_2[BO_2(OH)] (CNBB-$_3$)	300 W Xe, 20 mg sample, 2 mL deionized water, 1.7 g Na2CO3, 15 mL H2SO4	CO: 6.09	Pristine g-C_3N_4 CO: 2.19	Pristine g-C_3N_4 2.78		[219]
29	Type-II heterojunction of $Zn_{0.2}Cd_{0.8}S$/g-C_3N_4	300 W Xe, 80 °C, 0.6 MPa, 10 mg catalyst, 20 mL H_2O	CH_3OH: 11.5 ± 0.3	$Zn_{0.2}Cd_{0.8}S$: CH_3OH: 4.4 ± 0.2 g-C3N4: CH_3OH: 4.2 ± 0.1	$Zn_{0.2}$ $Cd_{0.8}S$: 2.6 g-C_3N_4: 2.7		[220]
30	3ZIF/1.5Au-PCN	300 W Xe, 0.1 g, 50 mL H_2O	CO: >10 CH4: >4		Pristine g-C_3N_4 8		[221]
31	TPVT-MOFs@g-C_3N_4-10	LED light, 1 mg, 1 mL dichloromethane	CO: 56.4	Pure g-C_3N_4: 17.5	Pure g-C_3N_4 3.2		[114]
32	NH2-MIL-101(Fe)/g-C3N4-30 wt%	300 W Xe, 2 mg	CO: 132.8	g-C_3N_4: 19.2	g-C_3N_4 6.9		[222]

4.3. Degradation of Organic Pollutants

Along with rapid population growth and significant industrialization development, large numbers of toxic, hazardous, and endless contaminants invade the environment, threatening to human life, especially a variety of pollutants present in water that are difficult to eliminate or degrade naturally. Photocatalytic degradation of contaminants is a green and efficient technology for coping with sewage [128,223]. Different kinds of g-C_3N_4-based materials (Table 3) have been exploited to increase the photodecomposition efficiency of pollutants, such as the constructed heterojunction, loading O_2-reduction co-catalysts, g-C_3N_4/CDs-based nanocomposites, and so on [182,224–226]. Generally, under the irradiation of visible light, the photogenerated electrons (e^-) on the g-C_3N_4 catalyst will be excited from VB to CB, leaving holes (h^+) in the VB. The holes can oxidize pollutants directly or react with H_2O/OH^- to form hydroxyl radicals [227]. When the REDOX potential of g-C_3N_4 composites is more negative than $O_2/O_2{}^-$, the photogenerated electrons in the material can react with O_2 to produce $O_2{}^-$ with strong oxidation capacity [228]. In addition, the resulting $O_2{}^-$ could be protonated to produce OH [229]. Finally, the RhB dye is degraded to CO_2 and H_2O under the action of these free radicals (Figure 14). Chen et al. [230] fabricated a $BiFeO_3$/g-C_3N_4 heterostructure through mixing-calcining and compared its performance with $BiFeO_3$. Around 30% higher photocatalytic efficiency toward RhB dye was observed for the $BiFeO_3$/10% g-C_3N_4 heterostructure, which was assigned to the contribution of a higher concentration of $O_2{}^-$. Zhang et al. [231] studied the selective reduction of molecular oxygen on g-C_3N_4 and probed its effect on the photocatalytic phenol degradation process. Compared with bulk g-C_3N_4, the exfoliated nanosheet yielded a three times improvement in photocatalytic phenol degradation. It has been demonstrated that bulk g-C_3N_4 prefers to reduce O_2 to $O_2{}^-$via one-electron reduction. At the same time, the photoexcited g-C_3N_4 nanosheet facilitates the two-electron reduction of O_2 to yield H_2O_2 because of the formation of 1,4-endoperoxide species. The two-electron reduction of O_2 on the nanosheet surface boosts hole generation and thus accelerates phenol oxidation degradation [231,232]. Thus, to improve the photocatalytic performance of g-C_3N_4, more effort should be devoted to strengthening the solid O_2-reduction reactions. For example, Liu et al. [83] reported a heterojunction material of K-doped g-C_3N4 nanosheet -CdS and degraded tetracycline with 94% degradation under visible light in 30 min. In addition, due to the electronegativities, ionic radius differences, and impurity states, element doping is

also an effective method to manipulate the electronic structure and physicochemical performance of g-C_3N_4-based materials. Gao et al. [68] synthesized Fe-doped g-C_3N_4 nanosheets and obtained 1.4- and 1.7-fold higher degradation rates of MB than that of pure g-C_3N_4 nanosheets and bulk g-C_3N_4, which indicated that the exploitation of efficient g-C_3N_4-based photocatalysts with high stabilization and degradation under visible light irradiation would significantly contribute to sewage disposal. Zhang et al. [117] synthesized a novel hybrid of Zr-based metal-organic framework with g-C_3N_4 (UiO-66/g-C_3N_4) nanosheets and applied a photodegradation of methylene blue, by which a 100% photodegradation was achieved within 4 h under visible light. This research has provided a new insight into the design of g-C_3N_4-based photocatalysts to deal with organic dyes in the environment.

Table 3. Photocatalytic degradation of pollutants over g-C_3N_4-based materials reported within the last three years.

Entry	Photocatalyst	Pollutant Concentration	Light Source	Degradation Efficiency/%	Ref.
1	5% g-C_3N_4-TiO_2	Acetaminophen: 0.033 mM	300 W Xe (>400 nm)	99.3 in 30 min	[233]
2	3ZIF/1.5Au-PCN	Bisphenol A	350 W Xe (>420 nm)	>85%	[221]
3	Cu(tmpa)/20%CN	Congo red: 100 mg·L^{-1}	150 W Xe	98.2% in 3 min	[234]
4	BiO-Ag(0)/C_3N_4@ ZIF-67	Congo red: 12 mg·L^{-1}	Natural sunlight	90% in 150 min	[13]
5	C_3N_4/RGO/$Bi_2Fe_4O_9$	Congo red: 10 mg·L^{-1}	LED 30 W	87.65% in 60 min	[235]
6	g-C_3N_4/Co-MOF	Crystal violet: 4 ppm	MaX 303 solar simulator (50 mW/cm)	95% in 80 min	[141]
7	Honeycomb-like g-C_3N_4/CeO_2-x	Cr (VI): 20 mg·L^{-1}	300 W Xe (>420 nm)	98% in 150 min	[236]
8	Sm_6WO_{12}/g-C_3N_4	Levofloxacin: 10 mg·L^{-1}	150 Mw cm^{-2} tungsten lamp	98% in 70 min	[237]
9	O-g/C_3N_4	Lincomycin: 100 mg·L^{-1}	PCX50C system (>420 nm)	99% within 3 h	[238]
10	ZnO-modified g-C_3N_4	Methylene blue: 10 ppm	200 W tungsten lamp (>420 nm)	97% in 80 min	[239]
11	Wood-like g-C_3N_4@WDC	Methylene blue: 20 mg·L^{-1}	300 W Xe (>400 nm)	98% in 60 min	[240]
12	BiO-Ag(0)/C_3N_4@ ZIF-67	Methylene blue: 12 mg·L^{-1}	Natural sunlight	96.5% in 120 min	[13]
13	Cerium-based GO/g-C_3N_4/Fe_2O_3	Methylene blue: 10 mg·L^{-1}	Light bulb	70.61% in 45 min	[14]
14	Ytterbium oxide-based GO/g-C_3N_4/Fe_2O_3	Methylene blue: 10 mg·L^{-1}	Light bulb	83.5% in 45 min	[14]
15	Cu(tmpa)/20%CN	Methylene blue: 10 mg·L^{-1}	150W Xe	92.0% within 20 min	[234]
16	C_3N_{4x}/AgO_y@$Co_{1-x}Bi_{1-y}O_7$	Methylene blue: 25 mL 10 mM	100 W tungsten bulb	96.4% in 120 min	[12]
17	Ternary composites of Zr-MOF combined with g-C3N4 and Ag_3PO_4	Methylene blue: 10 mg·L^{-1}	85-watt tungsten lamp outdoor/solar light in an open air	95% within 240 93% within 105 min	[241]
18	PSCN/Ag@AgI/WO_3	Malachite green: 1×10^{-4} mol dm^{-3}	35 W LED	90% in 60 min	[242]
19	Cu(tmpa)/20%CN	Malachite green: 30 mg·L^{-1}	150W Xe	92.9% in 35 min	[234]
20	20% g-C_3N_4/$Bi_4O_5I_2$	Methyl orange: 20 mg·L^{-1}	350 W Xe	0.164 min^{-1}	[243]
21	Cu(tmpa)/20%CN	Methyl violet: 10 mg·L^{-1}	150W Xe	92.0% in 60 min	[234]
22	$MnCo_2O_4$/g-C_3N_4	Nitrobenzene: 40 mg L^{-1}	CMCN2/PMS system	96.7% in 240 min	[244]
23	C_3N_{4x}/AgO_y@$Co_{1-x}Bi_{1-y}O_7$	Oxytetracycline: 25 mL 25 mM	100 W tungsten bulb	93% in 160 min	[12]
24	g-C_3N_4/WO_3/WS_2	Rhodamine B: 25 mg L^{-1}	300 W Xe (>420 nm)	96.2% in 20 min	[167]
25	Flower-like $Bi_{12}TiO_{20}$/g-C_3N_4	Rhodamine B: 20 mg·L^{-1}	150 mW·cm^{-2} Xe (>420 nm)	100% in 30 min	[245]
26	CdS/CQDs/g-C_3N_4	Rhodamine B: 10 mg·L^{-1}	300 W Xe (>420 nm)	100% in 20 min	[246]
27	Ytterbium oxide-based GO/g-C_3N_4/Fe_2O_3	Rhodamine B: 10 mg·L^{-1}	Light bulb	67.11% in 45 min	[14]
28	Cerium-based GO/g-C_3N_4/Fe_2O_3	Rhodamine B: 10 mg·L^{-1}	Light bulb	63.08% in 45 min	[14]
29	Fish-scale g-C_3N_4/$ZnIn_2S_4$	Tetracycline: 10 mg·L^{-1}	300 W Xe (>420 nm)	74% in 30 min	[247]
31	Flower-like Co_3O_4/g-C_3N_4	Tetracycline: 15 mg·L^{-1}	350 W Xe (>420 nm)	85.32% in 120 min	[248]
31	10 wt% $CuAl_2O_4$/g-C_3N_4	Tetracycline hydrochloride: 100 mg·L^{-1}	300 W Xe (>400 nm)	89.6% in 60 min	[249]
32	CO-C_3N_4	Tetracycline hydrochloride: 10 mg·L^{-1}	300 W Xe (>420 nm)	97.77% (PMS) in 40 min	[250]
33	ZIF-67/g-C_3N_4	Venlafaxine: 10 mg·L^{-1}	-	27.75% within 120 min	[251]
34	ZIF-67/MIL-100(Fe)/g-C_3N_4	Venlafaxine: 10 mg·L^{-1}	-	100% within 120 min	[251]
35	ZIF-67/MOF-74(Ni)/g-C_3N_4	Venlafaxine: 10 mg·L^{-1}	-	91.8% within 120 min	[251]

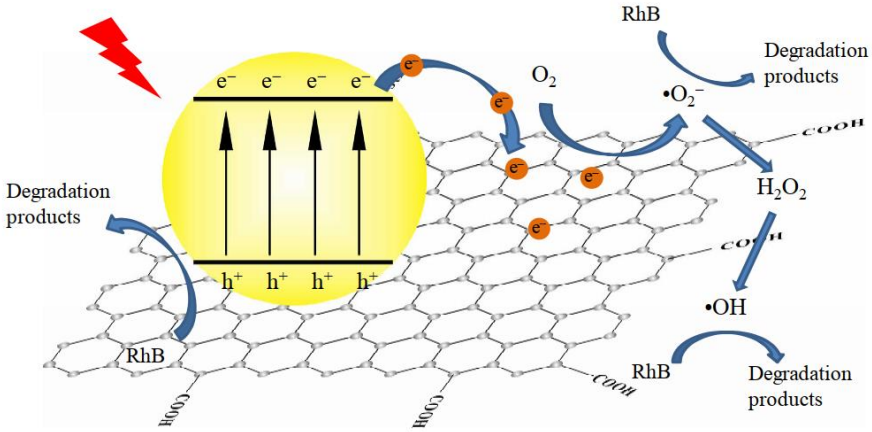

Figure 14. Photocatalytic mechanism of g-C_3N_4/rGO (reduced graphene oxide) for the degradation of Rhodamine B. Reprinted with permission from Ref. [122]. Copyright 2015 Elsevier.

5. Conclusions and Future Perspective

g-C_3N_4-based materials are still a research hotspot in photocatalysis, especially their application in energy and environmental sustainability. Although significant progress has been achieved in the preparation and modification of g-C_3N_4, several issues remain to be resolved in future research: (1) Some preparation methods are neither environmentally friendly nor time-saving. Thus, it is necessary to develop green and facile synthesis routes. For example, it should be encouraged to use plant leaves, natural halloysite, and some natural raw materials in the preparation of g-C_3N_4-based materials. (2) The absorption ability of available g-C_3N_4-based materials to visible and near-infrared light is still low, which is not beneficial to improving solar energy utilization. Coupling g-C_3N_4 with visible and near-infrared CDs might be an effective strategy. It would efficaciously improve the e^-/h^+ pair separation capability and visible light harnessing capability, thus enhancing the related photocatalytic performance. (3) Some structures of modified g-C_3N_4-base materials are complex, and the corresponding photocatalytic reaction mechanisms is not clear yet. Introducing density functional theory could provide insights into the photocatalytic mechanisms via disclosing the materials' structural, electronic, optical, and other properties. Detailed reaction processes can be performed by using in situ monitoring techniques (e.g., in situ infrared spectroscopy and mass spectrometry) to capture the reactive intermediates. (4) Although microscopic techniques and time-resolved spectroscopy have achieved the study of the steady-state charge distribution and charge transfer dynamics of photocatalysts, tracking the spatiotemporally evolving charge transfer processes in single photocatalyst particles and elaborating their exact mechanism is still a great challenge. Thus, it is significant to develop techniques to map holistic charge transfer processes at the single-particle level, identify where charges go and reveal how long they live on different sites. (5) Finally, the integration of artificial intelligence (AI) and other interdisciplinary techniques will play a tremendous driving role in precisely designing g-C_3N_4-based photocatalysts with excellent performance. For example, AI models could be developed to correlate photocatalytic performance with experimental conditions, which may help predict the photocatalytic performance of g-C_3N_4-based materials, improve the trial-and-error paradigm, and design new composite structures.

Author Contributions: Conceptualization of the review, Q.W. and F.H.; writing—original draft preparation, Q.W., Y.L. and S.S.; writing—review and editing, G.A., X.X. and B.Z.; supervision, Y.Z. and Z.Z. All authors have read and agreed to the published version of the manuscript.

Funding: This research was funded by the Natural Science Basic Research Program of Shaanxi Province of China (Grant No. 2021GY-247, 2019JC-33, and 2023-JC-QN-0122), National Natural Science Foundation of China (No. 22274128), the Youth Innovation Team of Shaanxi Universities (Grant No. Z19257), and China Postdoctoral Science Foundation (Grant No. 2022MD723840).

Institutional Review Board Statement: Not applicable.

Informed Consent Statement: Not applicable.

Data Availability Statement: Not applicable.

Acknowledgments: Not applicable.

Conflicts of Interest: The author declares no conflict of interest.

References

1. Li, W.; Sohail, M.; Anwar, U.; Taha, T.; Al-Sehemi, A.G.; Muhammad, S.; Al-Ghamdi, A.A.; Amin, M.A.; Palamanit, A.; Ullah, S. Recent progress in g–C_3N_4–based materials for remarkable photocatalytic sustainable energy. *Int. J. Hydrogen Energy* **2022**, *47*, 21067–21118. [CrossRef]
2. Meng, A.; Zhang, L.; Cheng, B.; Yu, J. Dual cocatalysts in TiO_2 photocatalysis. *Adv. Mater.* **2019**, *31*, 1807660. [CrossRef] [PubMed]
3. Xinchen, W.; Maeda, K.; Thomas, A.; Takanabe, K.; Gang, X.; Carlsson, J.; Domen, K.; Antonietti, M. A metal-free polymeric photocatalyst for hydrogen production from water under visible light. *Nat. Mater.* **2009**, *8*, 76–80.
4. Zhu, H.; Cai, S.; Liao, G.; Gao, Z.F.; Min, X.; Huang, Y.; Jin, S.; Xia, F. Recent advances in photocatalysis based on bioinspired superwettabilities. *ACS Catal.* **2021**, *11*, 14751–14771. [CrossRef]
5. Xing, Y.; Wang, X.; Hao, S.; Zhang, X.; Wang, X.; Ma, W.; Zhao, G.; Xu, X. Recent advances in the improvement of g-C_3N_4 based photocatalytic materials. *Chin. Chem. Lett.* **2021**, *32*, 13–20. [CrossRef]
6. Ismael, M. A review on graphitic carbon nitride (g-C_3N_4) based nanocomposites: Synthesis, categories, and their application in photocatalysis. *J. Alloys Compd.* **2020**, *846*, 156446. [CrossRef]
7. Meng, A.; Wu, S.; Cheng, B.; Yu, J.; Xu, J. Hierarchical TiO_2/Ni $(OH)_2$ composite fibers with enhanced photocatalytic CO_2 reduction performance. *J. Mater. Chem. A* **2018**, *6*, 4729–4736. [CrossRef]
8. Li, Y.; Zhou, M.; Cheng, B.; Shao, Y. Recent advances in g-C_3N_4-based heterojunction photocatalysts. *J. Mater. Sci. Technol.* **2020**, *56*, 1–17. [CrossRef]
9. Patnaik, S.; Sahoo, D.P.; Parida, K. Recent advances in anion doped g-C_3N_4 photocatalysts: A review. *Carbon* **2021**, *172*, 682–711. [CrossRef]
10. Govindasamy, P.; Kandasamy, B.; Thangavelu, P.; Barathi, S.; Thandavarayan, M.; Shkir, M.; Lee, J. Biowaste derived hydroxyapatite embedded on two-dimensional g-C_3N_4 nanosheets for degradation of hazardous dye and pharmacological drug via Z-scheme charge transfer. *Sci. Rep.* **2022**, *12*, 11572. [CrossRef]
11. Ye, L.; Liu, J.; Jiang, Z.; Peng, T.; Zan, L. Facets coupling of BiOBr-g-C_3N_4 composite photocatalyst for enhanced visible-light-driven photocatalytic activity. *Appl. Catal. B Environ.* **2013**, *142*, 1–7. [CrossRef]
12. Kumar, O.P.; Shahzad, K.; Nazir, M.A.; Farooq, N.; Malik, M.; Shah, S.S.A.; Ur Rehman, A. Photo-Fenton activated C_3N_{4x}/AgO_y@ $Co_{1-x}Bi_{0.\ 1-y}O_7$ dual s-scheme heterojunction towards degradation of organic pollutants. *Opt. Mater.* **2022**, *126*, 112199. [CrossRef]
13. Kumar, O.P.; Ahmad, M.; Nazir, M.A.; Anum, A.; Jamshaid, M.; Shah, S.S.A.; Rehman, A. Strategic combination of metal–organic frameworks and C_3N_4 for expeditious photocatalytic degradation of dye pollutants. *Environ. Sci. Pollut. Res.* **2022**, *29*, 35300–35313. [CrossRef] [PubMed]
14. Farooq, N.; Luque, R.; Hessien, M.M.; Qureshi, A.M.; Sahiba, F.; Nazir, M.A.; Ur Rehman, A. A comparative study of cerium-and ytterbium-based GO/g-C_3N_4/Fe_2O_3 composites for electrochemical and photocatalytic applications. *Appl. Sci.* **2021**, *11*, 9000. [CrossRef]
15. Wang, X.; Chen, X.; Thomas, A.; Fu, X.; Antonietti, M. Metal-containing carbon nitride compounds: A new functional organic–metal hybrid material. *Adv. Mater.* **2009**, *21*, 1609–1612. [CrossRef]
16. Ye, S.; Wang, R.; Wu, M.; Yuan, Y. A review on g-C_3N_4 for photocatalytic water splitting and CO_2 reduction. *Appl. Surf. Sci.* **2015**, *358*, 15–27. [CrossRef]
17. Wang, J.; Wang, S. A critical review on graphitic carbon nitride (g-C_3N_4)-based materials: Preparation, modification and environmental application. *Coord. Chem. Rev.* **2022**, *453*, 214338. [CrossRef]
18. Liebig, J.v. About some nitrogen compounds. *Ann. Pharm.* **1834**, *10*, 10.
19. Zhu, J.; Xiao, P.; Li, H.; Carabineiro, S.A. Graphitic carbon nitride: Synthesis, properties, and applications in catalysis. *ACS Appl. Mater. Interfaces* **2014**, *6*, 16449–16465. [CrossRef]
20. Franklin, E.C. The ammono carbonic acids. *J. Am. Chem. Soc.* **1922**, *44*, 486–509. [CrossRef]
21. Pauling, L.; Sturdivant, J. The structure of cyameluric acid, hydromelonic acid and related substances. *Proc. Natl. Acad. Sci. USA* **1937**, *23*, 615–620. [CrossRef] [PubMed]
22. Liu, A.Y.; Cohen, M.L. Prediction of new low compressibility solids. *Science* **1989**, *245*, 841–842. [CrossRef] [PubMed]
23. David, M.T.; Russell, J.H. Low-compressibility carbon nitrides. *Science* **1996**, *271*, 53–55.
24. Maya, L.; Cole, D.R.; Hagaman, E.W. Carbon–nitrogen pyrolyzates: Attempted preparation of carbon nitride. *J. Am. Ceram. Soc.* **1991**, *74*, 1686–1688. [CrossRef]
25. Wang, S.; Zhang, J.; Li, B.; Sun, H.; Wang, S. Engineered graphitic carbon nitride-based photocatalysts for visible-light-driven water splitting: A review. *Energy Fuels* **2021**, *35*, 6504–6526. [CrossRef]

26. Zhang, Q.; Xiang, X.; Ge, Y.; Yang, C.; Zhang, B.; Deng, K. Selectivity enhancement in the g-C_3N_4-catalyzed conversion of glucose to gluconic acid and glucaric acid by modification of cobalt thioporphyrazine. *J. Catal.* **2020**, *388*, 11–19. [CrossRef]
27. Su, F.; Mathew, S.C.; Lipner, G.; Fu, X.; Antonietti, M.; Blechert, S.; Wang, X. mpg-C_3N_4-catalyzed selective oxidation of alcohols using O_2 and visible light. *J. Am. Chem. Soc.* **2010**, *132*, 16299–16301. [CrossRef]
28. Balakrishnan, A.; Chinthala, M. Comprehensive review on advanced reusability of g-C_3N_4 based photocatalysts for the removal of organic pollutants. *Chemosphere* **2022**, *297*, 134190. [CrossRef]
29. Dong, G.; Zhang, Y.; Pan, Q.; Qiu, J. A fantastic graphitic carbon nitride (g-C3N4) material: Electronic structure, photocatalytic and photoelectronic properties. *J. Photochem. Photobiol. C Photochem. Rev.* **2014**, *20*, 33–50. [CrossRef]
30. Yan, S.; Li, Z.; Zou, Z. Photodegradation performance of g-C3N4 fabricated by directly heating melamine. *Langmuir* **2009**, *25*, 10397–10401. [CrossRef]
31. Liu, J.; Zhang, T.; Wang, Z.; Dawson, G.; Chen, W. Simple pyrolysis of urea into graphitic carbon nitride with recyclable adsorption and photocatalytic activity. *J. Mater. Chem.* **2011**, *21*, 14398–14401. [CrossRef]
32. Wu, X.; Chen, F.; Wang, X.; Yu, H. In situ one-step hydrothermal synthesis of oxygen-containing groups-modified g-C3N4 for the improved photocatalytic H2-evolution performance. *Appl. Surf. Sci.* **2018**, *427*, 645–653. [CrossRef]
33. Ahmad, I.; Danish, M.; Khan, A.; Muneer, M. One-pot hydrothermal synthesis of a double Z-scheme g-C_3N_4/AgI/β-$AgVO_3$ ternary nanocomposite for efficient degradation of organic pollutants and DPC–Cr (VI) complex under visible-light irradiation. *Photochem. Photobiol. Sci.* **2022**, *21*, 1371–1386. [CrossRef] [PubMed]
34. Sun, J.; Zhang, J.; Zhang, M.; Antonietti, M.; Fu, X.; Wang, X. Bioinspired hollow semiconductor nanospheres as photosynthetic nanoparticles. *Nat. Commun.* **2012**, *3*, 1139. [CrossRef]
35. Zhao, S.; Zhang, Y.; Zhou, Y.; Wang, Y.; Qiu, K.; Zhang, C.; Fang, J.; Sheng, X. Facile one-step synthesis of hollow mesoporous g-C_3N_4 spheres with ultrathin nanosheets for photoredox water splitting. *Carbon* **2018**, *126*, 247–256. [CrossRef]
36. Bai, G.; Song, Z.; Geng, H.; Gao, D.; Liu, K.; Wu, S.; Rao, W.; Guo, L.; Wang, J. Oxidized quasi-carbon nitride quantum dots inhibit ice growth. *Adv. Mater.* **2017**, *29*, 1606843. [CrossRef]
37. Chen, X.; Liu, Q.; Wu, Q.; Du, P.; Zhu, J.; Dai, S.; Yang, S. Incorporating graphitic carbon nitride (g-C_3N_4) quantum dots into bulk-heterojunction polymer solar cells leads to efficiency enhancement. *Adv. Funct. Mater.* **2016**, *26*, 1719–1728. [CrossRef]
38. Liu, Q.; Zhu, D.; Guo, M.; Yu, Y.; Cao, Y. Facile and efficient fabrication of g-C_3N_4 quantum dots for fluorescent analysis of trace copper (II) in environmental samples. *Chin. Chem. Lett.* **2019**, *30*, 1639–1642. [CrossRef]
39. Yousefzadeh, S.; Morovati, N. Modification of the ultrasonication derived-g-C_3N_4 nanosheets/quantum dots by MoS_2 nanostructures to improve electrocatalytic hydrogen evolution reaction. *Int. J. Hydrogen Energy* **2020**, *45*, 33512–33520. [CrossRef]
40. Li, C.; Sun, T.; Zhang, D.; Zhang, X.; Zhang, Y.; Lin, X.; Liu, J.; Zhu, L.; Wang, X.; Shi, Z. Microwave assisted-polymerization synthesis of 0D/2D CNQDs/g-C_3N_4 with the excellent visible light photocatalytic performance. *Mater. Lett.* **2022**, *308*, 131232. [CrossRef]
41. Wang, W.; Jimmy, C.Y.; Shen, Z.; Chan, D.K.; Gu, T. g-C_3N_4 quantum dots: Direct synthesis, upconversion properties and photocatalytic application. *Chem. Commun.* **2014**, *50*, 10148–10150. [CrossRef] [PubMed]
42. Dayal, S.; Burda, C. Surface effects on quantum dot-based energy transfer. *J. Am. Chem. Soc.* **2007**, *129*, 7977–7981. [CrossRef] [PubMed]
43. Chen, Q.; Tong, R.; Chen, X.; Xue, Y.; Xie, Z.; Kuang, Q.; Zheng, L. Ultrafine ZnO quantum dot-modified TiO_2 composite photocatalysts: The role of the quantum size effect in heterojunction-enhanced photocatalytic hydrogen evolution. *Catal. Sci. Technol.* **2018**, *8*, 1296–1303. [CrossRef]
44. Yeo, I.; Malik, N.S.; Munsch, M.; Dupuy, E.; Bleuse, J.; Niquet, Y.-M.; Gérard, J.-M.; Claudon, J.; Wagner, É.; Seidelin, S. Surface effects in a semiconductor photonic nanowire and spectral stability of an embedded single quantum dot. *Appl. Phys. Lett.* **2011**, *99*, 233106. [CrossRef]
45. Cui, Y.; Ding, Z.; Fu, X.; Wang, X. Construction of conjugated carbon nitride nanoarchitectures in solution at low temperatures for photoredox catalysis. *Angew. Chem. Int. Ed.* **2012**, *51*, 11814–11818. [CrossRef]
46. Wang, Q.; Shi, Y.; Du, Z.; He, J.; Zhong, J.; Zhao, L.; She, H.; Liu, G.; Su, B. Synthesis of rod-like g-C_3N_4/ZnS composites with superior photocatalytic activity for the degradation of methyl orange. *Eur. J. Inorg. Chem.* **2015**, *2015*, 4108–4115. [CrossRef]
47. Bai, X.; Wang, L.; Zong, R.; Zhu, Y. Photocatalytic activity enhanced via g-C_3N_4 nanoplates to nanorods. *J. Phys. Chem. C* **2013**, *117*, 9952–9961. [CrossRef]
48. Mo, Z.; Xu, H.; Chen, Z.; She, X.; Song, Y.; Wu, J.; Yan, P.; Xu, L.; Lei, Y.; Yuan, S. Self-assembled synthesis of defect-engineered graphitic carbon nitride nanotubes for efficient conversion of solar energy. *Appl. Catal. B Environ.* **2018**, *225*, 154–161. [CrossRef]
49. Jiang, Z.; Zhang, X.; Chen, H.S.; Hu, X.; Yang, P. Formation of g-C_3N_4 nanotubes towards superior photocatalysis performance. *ChemCatChem* **2019**, *11*, 4558–4567. [CrossRef]
50. Chen, D.; Wang, K.; Xiang, D.; Zong, R.; Yao, W.; Zhu, Y. Significantly enhancement of photocatalytic performances via core–shell structure of ZnO@ mpg-C_3N_4. *Appl. Catal. B Environ.* **2014**, *147*, 554–561. [CrossRef]
51. Zhou, Y.; Wang, Z.; Huang, L.; Zaman, S.; Lei, K.; Yue, T.; Li, Z.a.; You, B.; Xia, B.Y. Engineering 2D photocatalysts toward carbon dioxide reduction. *Adv. Energy Mater.* **2021**, *11*, 2003159. [CrossRef]
52. Niu, P.; Zhang, L.; Liu, G.; Cheng, H.M. Graphene-like carbon nitride nanosheets for improved photocatalytic activities. *Adv. Funct. Mater.* **2012**, *22*, 4763–4770. [CrossRef]

53. Liu, Q.; Wang, X.; Yang, Q.; Zhang, Z.; Fang, X. Mesoporous g-C_3N_4 nanosheets prepared by calcining a novel supramolecular precursor for high-efficiency photocatalytic hydrogen evolution. *Appl. Surf. Sci.* **2018**, *450*, 46–56. [CrossRef]
54. Qian, X.; Meng, X.; Sun, J.; Jiang, L.; Wang, Y.; Zhang, J.; Hu, X.; Shalom, M.; Zhu, J. Salt-assisted synthesis of 3D porous g-C_3N_4 as a bifunctional photo-and electrocatalyst. *ACS Appl. Mater. Interfaces* **2019**, *11*, 27226–27232. [CrossRef] [PubMed]
55. Toe, C.Y.; Tsounis, C.; Zhang, J.; Masood, H.; Gunawan, D.; Scott, J.; Amal, R. Advancing photoreforming of organics: Highlights on photocatalyst and system designs for selective oxidation reactions. *Energy Environ. Sci.* **2021**, *14*, 1140–1175. [CrossRef]
56. Gao, Y.; Zhao, W.; Zhang, D. Preparation of prismatic g-C_3N_4 by CTAB hydrothermal method and its degradation performance under visible light. *Diam. Relat. Mater.* **2022**, *121*, 108787. [CrossRef]
57. Lin, B.; Xia, M.; Xu, B.; Chong, B.; Chen, Z.; Yang, G. Bio-inspired nanostructured g-C_3N_4-based photocatalysts: A comprehensive review. *Chin. J. Catal.* **2022**, *43*, 2141–2172. [CrossRef]
58. Zhao, Z.; Wang, X.; Wang, S.; Xiao, Z.; Zhai, S.; Ma, J.; Dong, X.; Sun, H.; An, Q. Three-dimensional hierarchical seaweed-derived carbonaceous network with designed g-C_3N_4 nanosheets: Preparation and mechanism insight for 4-nitrophenol photoreduction. *Langmuir* **2022**, *38*, 11054–11067. [CrossRef]
59. Liu, Y.; Guo, X.; Chen, Z.; Zhang, W.; Wang, Y.; Zheng, Y.; Tang, X.; Zhang, M.; Peng, Z.; Li, R. Microwave-synthesis of g-C_3N_4 nanoribbons assembled seaweed-like architecture with enhanced photocatalytic property. *Appl. Catal. B Environ.* **2020**, *266*, 118624. [CrossRef]
60. Jiang, H.; Li, Y.; Wang, D.; Hong, X.; Liang, B. Recent advances in heteroatom doped graphitic carbon nitride (g-C_3N_4) and g-C_3N_4/metal oxide composite photocatalysts. *Curr. Org. Chem.* **2020**, *24*, 673–693. [CrossRef]
61. Liu, X.; Ma, R.; Zhuang, L.; Hu, B.; Chen, J.; Liu, X.; Wang, X. Recent developments of doped g-C_3N_4 photocatalysts for the degradation of organic pollutants. *Crit. Rev. Environ. Sci. Technol.* **2021**, *51*, 751–790. [CrossRef]
62. He, F.; Wang, Z.; Li, Y.; Peng, S.; Liu, B. The nonmetal modulation of composition and morphology of g-C_3N_4-based photocatalysts. *Appl. Catal. B Environ.* **2020**, *269*, 118828. [CrossRef]
63. Huang, Z.; Song, J.; Pan, L.; Wang, Z.; Zhang, X.; Zou, J.-J.; Mi, W.; Zhang, X.; Wang, L. Carbon nitride with simultaneous porous network and O-doping for efficient solar-energy-driven hydrogen evolution. *Nano Energy* **2015**, *12*, 646–656. [CrossRef]
64. Zhang, J.-W.; Gong, S.; Mahmood, N.; Pan, L.; Zhang, X.; Zou, J.-J. Oxygen-doped nanoporous carbon nitride via water-based homogeneous supramolecular assembly for photocatalytic hydrogen evolution. *Appl. Catal. B Environ.* **2018**, *221*, 9–16. [CrossRef]
65. She, X.; Liu, L.; Ji, H.; Mo, Z.; Li, Y.; Huang, L.; Du, D.; Xu, H.; Li, H. Template-free synthesis of 2D porous ultrathin nonmetal-doped g-C_3N_4 nanosheets with highly efficient photocatalytic H2 evolution from water under visible light. *Appl. Catal. B Environ.* **2016**, *187*, 144–153. [CrossRef]
66. Ma, X.; Lv, Y.; Xu, J.; Liu, Y.; Zhang, R.; Zhu, Y. A strategy of enhancing the photoactivity of g-C_3N_4 via doping of nonmetal elements: A first-principles study. *J. Phys. Chem. C* **2012**, *116*, 23485–23493. [CrossRef]
67. Wang, Y.; Zhao, S.; Zhang, Y.; Fang, J.; Zhou, Y.; Yuan, S.; Zhang, C.; Chen, W. One-pot synthesis of K-doped g-C_3N_4 nanosheets with enhanced photocatalytic hydrogen production under visible-light irradiation. *Appl. Surf. Sci.* **2018**, *440*, 258–265. [CrossRef]
68. Gao, J.; Wang, Y.; Zhou, S.; Lin, W.; Kong, Y. A facile one-step synthesis of Fe-doped g-C_3N_4 nanosheets and their improved visible-light photocatalytic performance. *ChemCatChem* **2017**, *9*, 1708–1715. [CrossRef]
69. Deng, P.; Shi, L.; Wang, H.; Qi, W. One-step preparation of novel K^+ and cyano-group co-doped crystalline polymeric carbon nitride with highly efficient H_2 evolution. *Colloids Surf. A Physicochem. Eng. Asp.* **2020**, *601*, 125023. [CrossRef]
70. Xu, L.; Zeng, J.; Li, Q.; Xia, L.; Luo, X.; Ma, Z.; Peng, B.; Xiong, S.; Li, Z.; Wang, L.-L. Defect-engineered 2D/2D hBN/g-C_3N_4 Z-scheme heterojunctions with full visible-light absorption: Efficient metal-free photocatalysts for hydrogen evolution. *Appl. Surf. Sci.* **2021**, *547*, 149207. [CrossRef]
71. Wang, M.; Jin, C.; Kang, J.; Liu, J.; Tang, Y.; Li, Z.; Li, S. CuO/g-C_3N_4 2D/2D heterojunction photocatalysts as efficient peroxymonosulfate activators under visible light for oxytetracycline degradation: Characterization, efficiency and mechanism. *Chem. Eng. J.* **2021**, *416*, 128118. [CrossRef]
72. Zhao, W.; Li, Y.; Zhao, P.; Zhang, L.; Dai, B.; Huang, H.; Zhou, J.; Zhu, Y.; Ma, K.; Leung, D.Y. Insights into the photocatalysis mechanism of the novel 2D/3D Z-Scheme g-C_3N_4/SnS_2 heterojunction photocatalysts with excellent photocatalytic performances. *J. Hazard. Mater.* **2021**, *402*, 123711. [CrossRef] [PubMed]
73. Wang, K.; Jiang, L.; Wu, X.; Zhang, G. Vacancy mediated Z-scheme charge transfer in a 2D/2D $La_2Ti_2O_7$/g-C_3N_4 nanojunction as a bifunctional photocatalyst for solar-to-energy conversion. *J. Mater. Chem. A* **2020**, *8*, 13241–13247. [CrossRef]
74. Chen, X.; Wang, J.; Chai, Y.; Zhang, Z.; Zhu, Y. Efficient photocatalytic overall water splitting induced by the giant internal electric field of ag-C_3N_4/rGO/PDIP Z-scheme heterojunction. *Adv. Mater.* **2021**, *33*, 2007479. [CrossRef] [PubMed]
75. Xu, H.; Wu, L.; Jin, L.; Wu, K. Combination mechanism and enhanced visible-light photocatalytic activity and stability of CdS/g-C_3N_4 heterojunctions. *J. Mater. Sci. Technol.* **2017**, *33*, 30–38. [CrossRef]
76. Liu, Y.; Li, X.; He, H.; Yang, S.; Jia, G.; Liu, S. CoP imbedded g-C_3N_4 heterojunctions for highly efficient photo, electro and photoelectrochemical water splitting. *J. Colloid Interface Sci.* **2021**, *599*, 23–33. [CrossRef] [PubMed]
77. Ma, J.; Zhou, W.; Tan, X.; Yu, T. Potassium ions intercalated into g-C_3N_4-modified TiO_2 nanobelts for the enhancement of photocatalytic hydrogen evolution activity under visible-light irradiation. *Nanotechnology* **2018**, *29*, 215706. [CrossRef]
78. Monsef, R.; Ghiyasiyan-Arani, M.; Salavati-Niasari, M. Design of magnetically recyclable ternary Fe_2O_3/EuVO4/g-C_3N_4 nanocomposites for photocatalytic and electrochemical hydrogen storage. *ACS Appl. Energy Mater.* **2021**, *4*, 680–695. [CrossRef]

79. Guo, F.; Huang, X.; Chen, Z.; Cao, L.; Cheng, X.; Chen, L.; Shi, W. Construction of Cu_3P-$ZnSnO_3$-g-C_3N_4 pnn heterojunction with multiple built-in electric fields for effectively boosting visible-light photocatalytic degradation of broad-spectrum antibiotics. *Sep. Purif. Technol.* **2021**, *265*, 118477. [CrossRef]
80. Li, K.; Chen, J.; Ao, Y.; Wang, P. Preparation of a ternary g-C_3N_4-CdS/$Bi_4O_5I_2$ composite photocatalysts with two charge transfer pathways for efficient degradation of acetaminophen under visible light irradiation. *Sep. Purif. Technol.* **2021**, *259*, 118177. [CrossRef]
81. Xiang, W.; Ji, Q.; Xu, C.; Guo, Y.; Liu, Y.; Sun, D.; Zhou, W.; Xu, Z.; Qi, C.; Yang, S. Accelerated photocatalytic degradation of iohexol over Co_3O_4/g-C_3N_4/$Bi_2O_2CO_3$ of pn/nn dual heterojunction under simulated sunlight by persulfate. *Appl. Catal. B Environ.* **2021**, *285*, 119847. [CrossRef]
82. Liu, S.; Li, F.; Li, Y.; Hao, Y.; Wang, X.; Li, B.; Liu, R. Fabrication of ternary g-C_3N_4/Al_2O_3/ZnO heterojunctions based on cascade electron transfer toward molecular oxygen activation. *Appl. Catal. B Environ.* **2017**, *212*, 115–128. [CrossRef]
83. Liu, Y.; Tian, J.; Wei, L.; Wang, Q.; Wang, C.; Xing, Z.; Li, X.; Yang, W.; Yang, C. Modified g-C_3N_4/TiO_2/CdS ternary heterojunction nanocomposite as highly visible light active photocatalyst originated from CdS as the electron source of TiO_2 to accelerate Z-type heterojunction. *Sep. Purif. Technol.* **2021**, *257*, 117976. [CrossRef]
84. Li, Z.; Huang, F.; Xu, Y.; Yan, A.; Dong, H.; Luo, S.; Hu, M. 2D/2D Nb_3O_7F/g-C_3N_4 heterojunction photocatalysts with enhanced hydrogen evolution activity. *ACS Appl. Energy Mater.* **2021**, *4*, 839–845. [CrossRef]
85. Shi, J.; Mao, L.; Cai, C.; Li, G.; Cheng, C.; Zheng, B.; Hu, Y.; Huang, Z.; Hu, X.; Żyła, G. One-pot fabrication of 2D/2D $HCa_2Nb_3O_{10}$/g-C_3N_4 type II heterojunctions towards enhanced photocatalytic H_2 evolution under visible-light irradiation. *Catal. Sci. Technol.* **2020**, *10*, 5896–5902. [CrossRef]
86. Bai, L.; Huang, H.; Zhang, S.; Hao, L.; Zhang, Z.; Li, H.; Sun, L.; Guo, L.; Huang, H.; Zhang, Y. Photocatalysis-assisted Co_3O_4/g-C_3N_4 p–n junction all-solid-state supercapacitors: A bridge between energy storage and photocatalysis. *Adv. Sci.* **2020**, *7*, 2001939. [CrossRef]
87. Vesali-Kermani, E.; Habibi-Yangjeh, A.; Diarmand-Khalilabad, H.; Ghosh, S. Nitrogen photofixation ability of g-C_3N_4 nanosheets/Bi_2MoO_6 heterojunction photocatalyst under visible-light illumination. *J. Colloid Interface Sci.* **2020**, *563*, 81–91. [CrossRef]
88. Kumaresan, N.; Sinthiya, M.M.A.; Sarathbavan, M.; Ramamurthi, K.; Sethuraman, K.; Babu, R.R. Synergetic effect of g-C_3N_4/ZnO binary nanocomposites heterojunction on improving charge carrier separation through 2D/1D nanostructures for effective photocatalytic activity under the sunlight irradiation. *Sep. Purif. Technol.* **2020**, *244*, 116356. [CrossRef]
89. Yan, T.; Liu, H.; Jin, Z. g-C_3N_4/α-Fe_2O_3 supported zero-dimensional Co_3S_4 nanoparticles form S-scheme heterojunction photocatalyst for efficient hydrogen production. *Energy Fuels* **2020**, *35*, 856–867. [CrossRef]
90. Fu, Y.; Zhang, Y.; Xie, X.; Wang, H.; Wei, L.; Ma, M.; Yan, Q. Functionalized carbon nanotube bridge interface drove $Bi_2O_2CO_3$/g-C_3N_4 S-scheme heterojunction with enhanced visible-light photocatalytic activity. *Sep. Purif. Technol.* **2021**, *274*, 119032. [CrossRef]
91. Guo, H.; Niu, C.-G.; Yang, Y.-Y.; Liang, C.; Niu, H.-Y.; Liu, H.-Y.; Li, L.; Tang, N. Interfacial Co-N bond bridged CoB/g-C_3N_4 Schottky junction with modulated charge transfer dynamics for highly efficient photocatalytic Staphylococcus aureus inactivation. *Chem. Eng. J.* **2021**, *422*, 130029. [CrossRef]
92. Lin, S.; Zhang, N.; Wang, F.; Lei, J.; Zhou, L.; Liu, Y.; Zhang, J. Carbon vacancy mediated incorporation of Ti_3C_2 quantum dots in a 3D inverse opal g-C_3N_4 Schottky junction catalyst for photocatalytic H_2O_2 production. *ACS Sustain. Chem. Eng.* **2020**, *9*, 481–488. [CrossRef]
93. Yi, X.; Yuan, J.; Tang, H.; Du, Y.; Hassan, B.; Yin, K.; Chen, Y.; Liu, X. Embedding few-layer Ti_3C_2Tx into alkalized g-C_3N_4 nanosheets for efficient photocatalytic degradation. *J. Colloid Interface Sci.* **2020**, *571*, 297–306. [CrossRef] [PubMed]
94. Ye, J.; Liu, J.; An, Y. Electric field and strain effects on the electronic and optical properties of g-C_3N_4/WSe_2 van der Waals heterostructure. *Appl. Surf. Sci.* **2020**, *501*, 144262. [CrossRef]
95. Xu, Q.; Zhang, L.; Cheng, B.; Fan, J.; Yu, J. S-scheme heterojunction photocatalyst. *Chem* **2020**, *6*, 1543–1559. [CrossRef]
96. Fu, J.; Xu, Q.; Low, J.; Jiang, C.; Yu, J. Ultrathin 2D/2D WO_3/g-C_3N_4 step-scheme H_2-production photocatalyst. *Appl. Catal. B Environ.* **2019**, *243*, 556–565. [CrossRef]
97. Ren, Y.; Li, Y.; Wu, X.; Wang, J.; Zhang, G. S-scheme Sb_2WO_6/g-C_3N_4 photocatalysts with enhanced visible-light-induced photocatalytic NO oxidation performance. *Chin. J. Catal.* **2021**, *42*, 69–77. [CrossRef]
98. Wang, J.; Wang, G.; Cheng, B.; Yu, J.; Fan, J. Sulfur-doped g-C_3N_4/TiO_2 S-scheme heterojunction photocatalyst for Congo Red photodegradation. *Chin. J. Catal.* **2021**, *42*, 56–68. [CrossRef]
99. Dai, Z.; Zhen, Y.; Sun, Y.; Li, L.; Ding, D. $ZnFe_2O_4$/g-C_3N_4 S-scheme photocatalyst with enhanced adsorption and photocatalytic activity for uranium (VI) removal. *Chem. Eng. J.* **2021**, *415*, 129002.
100. Mei, F.; Li, Z.; Dai, K.; Zhang, J.; Liang, C. Step-scheme porous g-C_3N_4/$Zn_{0.2}Cd_{0.8}S$-DETA composites for efficient and stable photocatalytic H_2 production. *Chin. J. Catal.* **2020**, *41*, 41–49. [CrossRef]
101. Xie, Q.; He, W.; Liu, S.; Li, C.; Zhang, J.; Wong, P.K. Bifunctional S-scheme g-C_3N_4/Bi/$BiVO_4$ hybrid photocatalysts toward artificial carbon cycling. *Chin. J. Catal.* **2020**, *41*, 140–153. [CrossRef]
102. Du, X.; Song, S.; Wang, Y.; Jin, W.; Ding, T.; Tian, Y.; Li, X. Facile one-pot synthesis of defect-engineered step-scheme WO_3/g-C_3N_4 heterojunctions for efficient photocatalytic hydrogen production. *Catal. Sci. Technol.* **2021**, *11*, 2734–2744. [CrossRef]
103. Wang, X.-J.; Tian, X.; Sun, Y.-J.; Zhu, J.-Y.; Li, F.-T.; Mu, H.-Y.; Zhao, J. Enhanced Schottky effect of a 2D–2D CoP/g-C_3N_4 interface for boosting photocatalytic H_2 evolution. *Nanoscale* **2018**, *10*, 12315–12321. [CrossRef]

104. She, X.; Xu, H.; Li, L.; Mo, Z.; Zhu, X.; Yu, Y.; Song, Y.; Wu, J.; Qian, J.; Yuan, S. Steering charge transfer for boosting photocatalytic H_2 evolution: Integration of two-dimensional semiconductor superiorities and noble-metal-free Schottky junction effect. *Appl. Catal. B Environ.* **2019**, *245*, 477–485. [CrossRef]
105. Yang, Y.; Zeng, Z.; Zeng, G.; Huang, D.; Xiao, R.; Zhang, C.; Zhou, C.; Xiong, W.; Wang, W.; Cheng, M. Ti_3C_2 Mxene/porous g-C_3N_4 interfacial Schottky junction for boosting spatial charge separation in photocatalytic H_2O_2 production. *Appl. Catal. B Environ.* **2019**, *258*, 117956. [CrossRef]
106. Shaheer, A.M.; Karthik, P.; Karthik, G.; Shankar, M.; Neppolian, B. Dual role of a g-C_3N_4/carbon intra-Schottky junction in charge carrier generation and separation for efficient solar H_2 production. *Catal. Sci. Technol.* **2019**, *9*, 3493–3503. [CrossRef]
107. Li, H.J.W.; Zhou, H.; Chen, K.; Liu, K.; Li, S.; Jiang, K.; Zhang, W.; Xie, Y.; Cao, Z.; Li, H. Metallic MoO_2-modified graphitic carbon nitride boosting photocatalytic CO_2 reduction via Schottky junction. *Solar Rrl* **2020**, *4*, 1900416. [CrossRef]
108. Sun, Z.; Fang, W.; Zhao, L.; Wang, H. 3D porous Cu-NPs/g-C_3N_4 foam with excellent CO_2 adsorption and Schottky junction effect for photocatalytic CO_2 reduction. *Appl. Surf. Sci.* **2020**, *504*, 144347. [CrossRef]
109. Li, J.; Zhang, Z.; Cui, W.; Wang, H.; Cen, W.; Johnson, G.; Jiang, G.; Zhang, S.; Dong, F. The spatially oriented charge flow and photocatalysis mechanism on internal van der Waals heterostructures enhanced g-C_3N_4. *ACS Catal.* **2018**, *8*, 8376–8385. [CrossRef]
110. Ran, J.; Guo, W.; Wang, H.; Zhu, B.; Yu, J.; Qiao, S.Z. Metal-free 2D/2D phosphorene/g-C_3N_4 Van der Waals heterojunction for highly enhanced visible-light photocatalytic H_2 production. *Adv. Mater.* **2018**, *30*, 1800128.
111. Sun, D.; Chi, D.; Yang, Z.; Xing, Z.; Yin, J.; Li, Z.; Zhu, Q.; Zhou, W. Mesoporous g-C_3N_4/Zn–Ti LDH laminated van der Waals heterojunction nanosheets as remarkable visible-light-driven photocatalysts. *Int. J. Hydrogen Energy* **2019**, *44*, 16348–16358. [CrossRef]
112. Dong, H.; Hong, S.; Zhang, P.; Yu, S.; Wang, Y.; Yuan, S.; Li, H.; Sun, J.; Chen, G.; Li, C. Metal-free Z-scheme 2D/2D VdW heterojunction for high-efficiency and durable photocatalytic H_2 production. *Chem. Eng. J.* **2020**, *395*, 125150. [CrossRef]
113. Song, X.; Wu, Y.; Zhang, X.; Li, X.; Zhu, Z.; Ma, C.; Yan, Y.; Huo, P.; Yang, G. Boosting charge carriers separation and migration efficiency via fabricating all organic van der Waals heterojunction for efficient photoreduction of CO_2. *Chem. Eng. J.* **2021**, *408*, 127292. [CrossRef]
114. Han, Z.; Fu, Y.; Zhang, Y.; Zhang, X.; Meng, X.; Zhou, Z.; Su, Z. Metal–organic framework (MOF) composite materials for photocatalytic CO_2 reduction under visible light. *Dalton Trans.* **2021**, *50*, 3186–3192. [CrossRef] [PubMed]
115. Zhang, X.; Yu, X.; Li, J.; Xu, L.; Li, B. Construction of MOFs/g-C_3N_4 composite for accelerating visible-light-driven hydrogen evolution. *Int. J. Hydrogen Energy* **2022**, *47*, 18007–18017. [CrossRef]
116. Lv, P.; Duan, F.; Sheng, J.; Lu, S.; Zhu, H.; Du, M.; Chen, M. The 2D/2D p–n heterojunction of ZnCoMOF/g-C_3N_4 with enhanced photocatalytic hydrogen evolution under visible light irradiation. *Appl. Organomet. Chem.* **2021**, *35*, e6124. [CrossRef]
117. Zhang, Y.; Zhou, J.; Feng, Q.; Chen, X.; Hu, Z. Visible light photocatalytic degradation of MB using UiO-66/g-C_3N_4 heterojunction nanocatalyst. *Chemosphere* **2018**, *212*, 523–532. [CrossRef]
118. Ma, X.; Li, X.; Li, M.; Ma, X.; Yu, L.; Dai, Y. Effect of the structure distortion on the high photocatalytic performance of C_{60}/g-C_3N_4 composite. *Appl. Surf. Sci.* **2017**, *414*, 124–130. [CrossRef]
119. Zhang, Y.; Wang, G.; Jin, Z. An orderly assembled g-C_3N_4, rGO and Ni_2P photocatalyst for efficient hydrogen evolution. *Int. J. Hydrogen Energy* **2019**, *44*, 10316–10327. [CrossRef]
120. Liu, J.; Song, Y.; Xu, H.; Zhu, X.; Lian, J.; Xu, Y.; Zhao, Y.; Huang, L.; Ji, H.; Li, H. Non-metal photocatalyst nitrogen-doped carbon nanotubes modified mpg-C_3N_4: Facile synthesis and the enhanced visible-light photocatalytic activity. *J. Colloid Interface Sci.* **2017**, *494*, 38–46. [CrossRef]
121. Cheng, L.; Zhang, H.; Li, X.; Fan, J.; Xiang, Q. Carbon–graphitic carbon nitride hybrids for heterogeneous photocatalysis. *Small* **2021**, *17*, 2005231. [CrossRef] [PubMed]
122. Yuan, B.; Wei, J.; Hu, T.; Yao, H.; Jiang, Z.; Fang, Z.; Chu, Z. Simple synthesis of g-C_3N_4/rGO hybrid catalyst for the photocatalytic degradation of rhodamine B. *Chin. J. Catal.* **2015**, *36*, 1009–1016. [CrossRef]
123. Ge, L.; Han, C. Synthesis of MWNTs/g-C_3N_4 composite photocatalysts with efficient visible light photocatalytic hydrogen evolution activity. *Appl. Catal. B Environ.* **2012**, *117*, 268–274. [CrossRef]
124. Wang, Q.; Feng, Z.; He, H.; Hu, X.; Mao, J.; Chen, X.; Liu, L.; Wei, X.; Liu, D.; Bi, S. Nonblinking carbon dots for imaging and tracking receptors on a live cell membrane. *Chem. Commun.* **2021**, *57*, 5554–5557.
125. Zhang, F.; Wen, Q.; Hong, M.; Zhuang, Z.; Yu, Y. Efficient and sustainable metal-free GR/C_3N_4/CDots ternary heterostructrues for versatile visible-light-driven photoredox applications: Toward synergistic interaction of carbon materials. *Chem. Eng. J.* **2017**, *307*, 593–603.
126. He, H.; Liu, L.; Chen, X.; Wang, Q.; Wang, X.; Nau, W.M.; Huang, F. Carbon dot blinking enables accurate molecular counting at nanoscale resolution. *Anal. Chem.* **2021**, *93*, 3968–3975. [CrossRef]
127. Liu, J.; Liu, Y.; Liu, N.; Han, Y.; Zhang, X.; Huang, H.; Lifshitz, Y.; Lee, S.-T.; Zhong, J.; Kang, Z. Metal-free efficient photocatalyst for stable visible water splitting via a two-electron pathway. *Science* **2015**, *347*, 970–974. [CrossRef]
128. Asadzadeh-Khaneghah, S.; Habibi-Yangjeh, A. g-C_3N_4/carbon dot-based nanocomposites serve as efficacious photocatalysts for environmental purification and energy generation: A review. *J. Clean. Prod.* **2020**, *276*, 124319. [CrossRef]
129. Fang, S.; Xia, Y.; Lv, K.; Li, Q.; Sun, J.; Li, M. Effect of carbon-dots modification on the structure and photocatalytic activity of g-C_3N_4. *Appl. Catal. B Environ.* **2016**, *185*, 225–232. [CrossRef]

130. Ai, L.; Shi, R.; Yang, J.; Zhang, K.; Zhang, T.; Lu, S. Efficient combination of g-C_3N_4 and CDs for enhanced photocatalytic performance: A review of synthesis, strategies, and applications. *Small* **2021**, *17*, 2007523. [CrossRef]
131. Yan, L.; Zhong, S.; Igou, T.; Gao, H.; Li, J.; Chen, Y. Development of machine learning models to enhance element-doped g-C_3N_4 photocatalyst for hydrogen production through splitting water. *Int. J. Hydrogen Energy* **2022**, *47*, 34075–34089. [CrossRef]
132. Sharma, R.; Almáši, M.; Nehra, S.P.; Rao, V.S.; Panchal, P.; Paul, D.R.; Jain, I.P.; Sharma, A. Photocatalytic hydrogen production using graphitic carbon nitride (GCN): A precise review. *Renew. Sustain. Energy Rev.* **2022**, *168*, 112776. [CrossRef]
133. Kar, S.; Bishwal, L.; Kommula, B.; Bhattacharyya, S. Critical optimization of phosphorus functionalized carbon nanomaterials for metal-free solar hydrogen production and simultaneous organic transformation. *Adv. Opt. Mater.* **2022**, *10*, 2102641. [CrossRef]
134. Gao, Y.; Hou, F.; Hu, S.; Wu, B.; Wang, Y.; Zhang, H.; Jiang, B.; Fu, H. Graphene quantum-dot-modified hexagonal tubular carbon nitride for visible-light photocatalytic hydrogen evolution. *ChemCatChem* **2018**, *10*, 1330–1335. [CrossRef]
135. Ling, G.Z.S.; Ng, S.F.; Ong, W.J. Tailor-engineered 2D cocatalysts: Harnessing electron–hole redox center of 2D g-C_3N_4 photocatalysts toward solar-to-chemical conversion and environmental purification. *Adv. Funct. Mater.* **2022**, *32*, 2111875. [CrossRef]
136. Shi, W.; Wang, J.; Yang, S.; Lin, X.; Guo, F.; Shi, J. Fabrication of a ternary carbon dots/CoO/g-C_3N_4 nanocomposite photocatalyst with enhanced visible-light-driven photocatalytic hydrogen production. *J. Chem. Technol. Biotechnol.* **2020**, *95*, 2129–2138. [CrossRef]
137. Zhang, S.; Gao, M.; Zhai, Y.; Wen, J.; Yu, J.; He, T.; Kang, Z.; Lu, S. Which kind of nitrogen chemical states doped carbon dots loaded by g-C_3N_4 is the best for photocatalytic hydrogen production. *J. Colloid Interface Sci.* **2022**, *622*, 662–674. [CrossRef]
138. Hussien, M.K.; Sabbah, A.; Qorbani, M.; Elsayed, M.H.; Raghunath, P.; Lin, T.-Y.; Quadir, S.; Wang, H.-Y.; Wu, H.-L.; Tzou, D.-L.M. Metal-free four-in-one modification of g-C_3N_4 for superior photocatalytic CO_2 reduction and H_2 evolution. *Chem. Eng. J.* **2022**, *430*, 132853. [CrossRef]
139. Li, L.; Wang, X.; Gu, H.; Zhang, H.; Zhang, J.; Zhang, Q.; Dai, W.-L. Which Is more efficient in promoting the photocatalytic H_2 evolution performance of g-C_3N_4: Monometallic nanocrystal, heterostructural nanocrystal, or bimetallic nanocrystal? *Inorg. Chem.* **2022**, *61*, 4760–4768. [CrossRef]
140. Sun, Y.; Kumar, V.; Kim, K.-H. The assessment of graphitic carbon nitride (g-C_3N_4) materials for hydrogen evolution reaction: Effect of metallic and non-metallic modifications. *Sep. Purif. Technol.* **2022**, *305*, 122413. [CrossRef]
141. Devarayapalli, K.; Vattikuti, S.P.; Sreekanth, T.; Yoo, K.S.; Nagajyothi, P.; Shim, J. Hydrogen production and photocatalytic activity of g-C_3N_4/Co-MOF (ZIF-67) nanocomposite under visible light irradiation. *Appl. Organomet. Chem.* **2020**, *34*, e5376. [CrossRef]
142. Yu, H.; Ma, H.; Wu, X.; Wang, X.; Fan, J.; Yu, J. One-step realization of crystallization and cyano-group generation for g-C_3N_4 photocatalysts with improved H_2 production. *Solar Rrl* **2021**, *5*, 2000372. [CrossRef]
143. Wang, K.; Li, Y.; Li, J.; Zhang, G. Boosting interfacial charge separation of $Ba_5Nb_4O_{15}$/g-C_3N_4 photocatalysts by 2D/2D nanojunction towards efficient visible-light driven H_2 generation. *Appl. Catal. B Environ.* **2020**, *263*, 117730. [CrossRef]
144. Katsumata, H.; Tateishi, I.; Furukawa, M.; Kaneco, S. Highly photocatalytic hydrogen generation over P-doped g-C_3N_4 with aromatic ring structure. *Mater. Lett.* **2021**, *299*, 130068. [CrossRef]
145. Xi, C.; Deng, P.; Miao, D.; Zhang, L.; Liu, W.; Hou, Y. Improved charge transfer by binary Ni_3S_2-NiS_2 for boosting the photocatalytic hydrogen generation over g-C3N4. *Mater. Lett.* **2022**, *307*, 131012. [CrossRef]
146. Liang, G.; Waqas, M.; Yang, B.; Xiao, K.; Li, J.; Zhu, C.; Zhang, J.; Duan, H. Enhanced photocatalytic hydrogen evolution under visible light irradiation by p-type MoS_2/n-type Ni_2P doped g-C_3N_4. *Appl. Surf. Sci.* **2020**, *504*, 144448. [CrossRef]
147. Nasir, M.S.; Yang, G.; Ayub, I.; Wang, X.; Wang, S.; Yan, W. Hybridization of g-C_3N_4 quantum dots with 1D branched TiO_2 fiber for efficient visible light-driven photocatalytic hydrogen generation. *Int. J. Hydrogen Energy* **2020**, *45*, 13994–14005. [CrossRef]
148. Samsudin, M.F.R.; Ullah, H.; Bashiri, R.; Mohamed, N.M.; Sufian, S.; Ng, Y.H. Experimental and DFT insights on microflower g-C_3N_4/$BiVO_4$ photocatalyst for enhanced photoelectrochemical hydrogen generation from lake water. *ACS Sustain. Chem. Eng.* **2020**, *8*, 9393–9403. [CrossRef]
149. Qi, K.; Lv, W.; Khan, I.; Liu, S.-y. Photocatalytic H2 generation via CoP quantum-dot-modified g-C_3N_4 synthesized by electroless plating. *Chin. J. Catal.* **2020**, *41*, 114–121. [CrossRef]
150. Ma, B.; Zhao, J.; Ge, Z.; Chen, Y.; Yuan, Z. 5 nm NiCoP nanoparticles coupled with g-C_3N_4 as high-performance photocatalyst for hydrogen evolution. *Sci. China Mater.* **2020**, *63*, 258–266. [CrossRef]
151. Jia, J.; Sun, W.; Zhang, Q.; Zhang, X.; Hu, X.; Liu, E.; Fan, J. Inter-plane heterojunctions within 2D/2D $FeSe_2$/g-C_3N_4 nanosheet semiconductors for photocatalytic hydrogen generation. *Appl. Catal. B Environ.* **2020**, *261*, 118249. [CrossRef]
152. Fan, Y.; Chen, H.; Cui, D.; Fan, Z.; Xue, C. $NiCo_2O_4$/g-C_3N_4 Heterojunction Photocatalyst for Efficient H_2 Generation. *Energy Technol.* **2021**, *9*, 2000973. [CrossRef]
153. Bi, Z.-x.; Guo, R.-t.; Ji, X.-y.; Hu, X.; Wang, J.; Chen, X.; Pan, W.-g. Direct Z-scheme CoS/g-C_3N_4 heterojunction with NiS co-catalyst for efficient photocatalytic hydrogen generation. *Int. J. Hydrogen Energy* **2022**, *47*, 34430–34443. [CrossRef]
154. Zada, A.; Khan, M.; Hussain, Z.; Shah, M.I.A.; Ateeq, M.; Ullah, M.; Ali, N.; Shaheen, S.; Yasmeen, H.; Shah, S.N.A. Extended visible light driven photocatalytic hydrogen generation by electron induction from g-C_3N_4 nanosheets to ZnO through the proper heterojunction. *Z. Phys. Chem.* **2022**, *236*, 53–66. [CrossRef]
155. Mehtab, A.; Banerjee, S.; Mao, Y.; Ahmad, T. Type-II $CuFe_2O_4$/graphitic carbon nitride heterojunctions for high-efficiency photocatalytic and electrocatalytic hydrogen generation. *ACS Appl. Mater. Interfaces* **2022**, *14*, 44317–44329. [CrossRef]
156. Mishra, B.P.; Babu, P.; Parida, K. Phosphorous, boron and sulfur doped g-C_3N_4 nanosheet: Synthesis, characterization, and comparative study towards photocatalytic hydrogen generation. *Mater. Today Proc.* **2021**, *35*, 258–262. [CrossRef]

157. Alhaddad, M.; Navarro, R.; Hussein, M.; Mohamed, R. Bi_2O_3/g-C_3N_4 nanocomposites as proficient photocatalysts for hydrogen generation from aqueous glycerol solutions beneath visible light. *Ceram. Int.* **2020**, *46*, 24873–24881. [CrossRef]
158. Ding, J.; Sun, X.; Wang, Q.; Li, D.-s.; Li, X.; Li, X.; Chen, L.; Zhang, X.; Tian, X.; Ostrikov, K.K. Plasma synthesis of Pt/g-C_3N_4 photocatalysts with enhanced photocatalytic hydrogen generation. *J. Alloys Compd.* **2021**, *873*, 159871. [CrossRef]
159. Jin, Z.; Li, Y.; Hao, X. Ni, Co-based selenide anchored g-C_3N_4 for boosting photocatalytic hydrogen evolution. *Acta Phys.-Chim. Sin.* **2021**, *37*, 1912033.
160. Nagaraja, C.; Kaur, M.; Dhingra, S. Enhanced visible-light-assisted photocatalytic hydrogen generation by MoS_2/g-C_3N_4 nanocomposites. *Int. J. Hydrogen Energy* **2020**, *45*, 8497–8506. [CrossRef]
161. Li, J.; Ma, W.; Chen, J.; An, N.; Zhao, Y.; Wang, D.; Mao, Z. Carbon vacancies improved photocatalytic hydrogen generation of g-C_3N_4 photocatalyst via magnesium vapor etching. *Int. J. Hydrogen Energy* **2020**, *45*, 13939–13946. [CrossRef]
162. Ma, X.; Luo, B.; Zeng, Z.; Hu, S.; Jing, D. Significantly Enhanced Photocatalytic Hydrogen Generation over a 2D/2D Z-Scheme La2NiO_4/g-C_3N_4 Hybrid Free of Noble Metal Cocatalyst. *ACS Appl. Energy Mater.* **2021**, *4*, 10721–10730. [CrossRef]
163. Che, Y.; Liu, Q.; Lu, B.; Zhai, J.; Wang, K.; Liu, Z. Plasmonic ternary hybrid photocatalyst based on polymeric g-C_3N_4 towards visible light hydrogen generation. *Sci. Rep.* **2020**, *10*, 721. [CrossRef] [PubMed]
164. Hou, X.; Cui, L.; Du, H.; Gu, L.; Li, Z.; Yuan, Y. Lowering the schottky barrier of g-C_3N_4/Carbon graphite heterostructure by N-doping for increased photocatalytic hydrogen generation. *Appl. Catal. B Environ.* **2020**, *278*, 119253. [CrossRef]
165. Rawool, S.A.; Samanta, A.; Ajithkumar, T.; Kar, Y.; Polshettiwar, V. Photocatalytic hydrogen generation and CO_2 conversion using g-C_3N_4 decorated dendritic fibrous nanosilica: Role of interfaces between silica and g-C3N4. *ACS Appl. Energy Mater.* **2020**, *3*, 8150–8158. [CrossRef]
166. Wan, C.; Zhou, L.; Sun, L.; Xu, L.; Cheng, D.-g.; Chen, F.; Zhan, X.; Yang, Y. Boosting visible-light-driven hydrogen evolution from formic acid over AgPd/2D g-C_3N_4 nanosheets Mott-Schottky photocatalyst. *Chem. Eng. J.* **2020**, *396*, 125229. [CrossRef]
167. Song, T.; Xie, C.; Matras-Postolek, K.; Yang, P. 2D layered g-C_3N_4/WO_3/WS_2 S-scheme heterojunctions with enhanced photochemical performance. *J. Phys. Chem. C* **2021**, *125*, 19382–19393. [CrossRef]
168. Zhao, W.; She, T.; Zhang, J.; Wang, G.; Zhang, S.; Wei, W.; Yang, G.; Zhang, L.; Xia, D.; Cheng, Z. A novel Z-scheme CeO_2/g-C_3N_4 heterojunction photocatalyst for degradation of Bisphenol A and hydrogen evolution and insight of the photocatalysis mechanism. *J. Mater. Sci. Technol.* **2021**, *85*, 18–29. [CrossRef]
169. Liao, Y.; Wang, G.; Wang, J.; Wang, K.; Yan, S.; Su, Y. Nitrogen vacancy induced in situ g-C_3N_4 pn homojunction for boosting visible light-driven hydrogen evolution. *J. Colloid Interface Sci.* **2021**, *587*, 110–120. [CrossRef]
170. Zhang, X.; Zhang, X.R.; Yang, P.; Chen, H.-S. Black magnetic Cu-g-C_3N_4 nanosheets towards efficient photocatalytic H_2 generation and CO_2/benzene conversion. *Chem. Eng. J.* **2022**, *450*, 138030. [CrossRef]
171. Zhao, B.; Xu, J.; Liu, Y.; Fan, J.; Yu, H. Amino group-rich porous g-C_3N_4 nanosheet photocatalyst: Facile oxalic acid-induced synthesis and improved H_2-evolution activity. *Ceram. Int.* **2021**, *47*, 18295–18303. [CrossRef]
172. Yuan, H.; Fang, F.; Dong, J.; Xia, W.; Zeng, X.; Shangguan, W. Enhanced photocatalytic hydrogen production based on laminated MoS_2/g-C_3N_4 photocatalysts. *Colloids Surf. A Physicochem. Eng. Asp.* **2022**, *641*, 128575. [CrossRef]
173. Kamat, P.V. Meeting the clean energy demand: Nanostructure architectures for solar energy conversion. *J. Phys. Chem. C* **2007**, *111*, 2834–2860. [CrossRef]
174. Wang, Q.; Fang, Z.; Zhang, W.; Zhang, D. High-efficiency g-C_3N_4 based photocatalysts for CO_2 reduction: Modification methods. *Adv. Fiber Mater.* **2022**, *4*, 342–360. [CrossRef]
175. Fu, J.; Yu, J.; Jiang, C.; Cheng, B. g-C3N4-based heterostructured photocatalysts. *Adv. Energy Mater.* **2018**, *8*, 1701503. [CrossRef]
176. Kumar, S.; Karthikeyan, S.; Lee, A.F. g-C_3N_4-based nanomaterials for visible light-driven photocatalysis. *Catalysts* **2018**, *8*, 74. [CrossRef]
177. Li, Y.; Kong, T.; Shen, S. Artificial photosynthesis with polymeric carbon nitride: When meeting metal nanoparticles, single atoms, and molecular complexes. *Small* **2019**, *15*, 1900772. [CrossRef]
178. Zhang, L.; Long, R.; Zhang, Y.; Duan, D.; Xiong, Y.; Zhang, Y.; Bi, Y. Direct observation of dynamic bond evolution in single-atom Pt/C_3N_4 catalysts. *Angew. Chem.* **2020**, *132*, 6283–6288. [CrossRef]
179. Liu, W.; Cao, L.; Cheng, W.; Cao, Y.; Liu, X.; Zhang, W.; Mou, X.; Jin, L.; Zheng, X.; Che, W. Single-site active cobalt-based photocatalyst with a Long carrier lifetime for spontaneous overall water splitting. *Angew. Chem.* **2017**, *129*, 9440–9445. [CrossRef]
180. Pan, Z.; Zheng, Y.; Guo, F.; Niu, P.; Wang, X. Decorating CoP and Pt nanoparticles on graphitic carbon nitride nanosheets to promote overall water splitting by conjugated polymers. *ChemSusChem* **2017**, *10*, 87–90. [CrossRef]
181. Reddy, K.R.; Reddy, C.V.; Nadagouda, M.N.; Shetti, N.P.; Jaesool, S.; Aminabhavi, T.M. Polymeric graphitic carbon nitride (g-C_3N_4)-based semiconducting nanostructured materials: Synthesis methods, properties and photocatalytic applications. *J. Environ. Manag.* **2019**, *238*, 25–40. [CrossRef] [PubMed]
182. Wen, J.; Xie, J.; Chen, X.; Li, X. A review on g-C_3N_4-based photocatalysts. *Appl. Surf. Sci.* **2017**, *391*, 72–123. [CrossRef]
183. Wang, K.; Li, Q.; Liu, B.; Cheng, B.; Ho, W.; Yu, J. Sulfur-doped g-C_3N_4 with enhanced photocatalytic CO_2-reduction performance. *Appl. Catal. B Environ.* **2015**, *176*, 44–52. [CrossRef]
184. Sun, Z.; Wang, H.; Wu, Z.; Wang, L. g-C_3N_4 based composite photocatalysts for photocatalytic CO_2 reduction. *Catal. Today* **2018**, *300*, 160–172. [CrossRef]
185. Ghosh, U.; Majumdar, A.; Pal, A. Photocatalytic CO_2 reduction over g-C_3N_4 based heterostructures: Recent progress and prospects. *J. Environ. Chem. Eng.* **2021**, *9*, 104631. [CrossRef]

186. Li, X.; Xiong, J.; Gao, X.; Huang, J.; Feng, Z.; Chen, Z.; Zhu, Y. Recent advances in 3D g-C_3N_4 composite photocatalysts for photocatalytic water splitting, degradation of pollutants and CO_2 reduction. *J. Alloys Compd.* **2019**, *802*, 196–209. [CrossRef]
187. Zhang, X. Layered g-C_3N_4/TiO_2 nanocomposites for efficient photocatalytic water splitting and CO_2 reduction: A review. *Mater. Today Energy* **2022**, *23*, 100904. [CrossRef]
188. Chen, P.; Dong, X.a.; Huang, M.; Li, K.; Xiao, L.; Sheng, J.; Chen, S.; Zhou, Y.; Dong, F. Rapid self-decomposition of g-C_3N_4 during gas–solid photocatalytic CO_2 reduction and its effects on performance assessment. *ACS Catal.* **2022**, *12*, 4560–4570. [CrossRef]
189. Li, H.; Wang, D.; Miao, C.; Wang, Y.; Wang, Y.; Liu, C.; Che, G. g-C_3N_4/BiOI S-scheme heterojunction: A 2D/2D model platform for visible-light-driven photocatalytic CO_2 reduction and pollutant degradation. *J. Environ. Chem. Eng.* **2022**, *10*, 108201. [CrossRef]
190. Fu, J.; Zhu, B.; Jiang, C.; Cheng, B.; You, W.; Yu, J. Hierarchical porous O-doped g-C_3N_4 with enhanced photocatalytic CO_2 reduction activity. *Small* **2017**, *13*, 1603938. [CrossRef]
191. Huo, Y.; Zhang, J.; Dai, K.; Liang, C. Amine-modified S-scheme porous g-C_3N_4/CdSe–diethylenetriamine composite with enhanced photocatalytic CO_2 reduction activity. *ACS Appl. Energy Mater.* **2021**, *4*, 956–968. [CrossRef]
192. Tang, R.; Wang, H.; Zhang, S.; Zhang, L.; Dong, F. A ball milling method for highly dispersed Ni atoms on g-C_3N_4 to boost CO_2 photoreduction. *J. Colloid Interface Sci.* **2023**, *630*, 290–300. [CrossRef] [PubMed]
193. Lu, Z.; Wang, Z. S-scheme $CuWO_4$@ g-C_3N_4 core-shell microsphere for CO_2 photoreduction. *Mater. Sci. Semicond. Process.* **2023**, *153*, 107177. [CrossRef]
194. Li, J.; He, C.; Xu, N.; Wu, K.; Huang, Z.; Zhao, X.; Nan, J.; Xiao, X. Interfacial bonding of hydroxyl-modified g-C_3N_4 and $Bi_2O_2CO_3$ toward boosted CO_2 photoreduction: Insights into the key role of OH groups. *Chem. Eng. J.* **2023**, *452*, 139191. [CrossRef]
195. Gao, Y.; Sun, L.; Bian, J.; Zhang, Z.; Li, Z.; Jing, L. Accelerated charge transfer of g-C_3N_4/$BiVO_4$ Z-scheme 2D heterojunctions by controllably introducing phosphate bridges and Ag nanocluster co-catalysts for selective CO_2 photoreduction to CO. *Appl. Surf. Sci.* **2023**, *610*, 155360. [CrossRef]
196. Wang, K.; Feng, X.; Shangguan, Y.; Wu, X.; Chen, H. Selective CO_2 photoreduction to CH_4 mediated by dimension-matched 2D/2D Bi_3NbO_7/g-C_3N_4 S-scheme heterojunction. *Chin. J. Catal.* **2022**, *43*, 246–254. [CrossRef]
197. Wang, J.; Yu, Y.; Cui, J.; Li, X.; Zhang, Y.; Wang, C.; Yu, X.; Ye, J. Defective g-C_3N_4/covalent organic framework van der Waals heterojunction toward highly efficient S-scheme CO_2 photoreduction. *Appl. Catal. B Environ.* **2022**, *301*, 120814. [CrossRef]
198. Tao, K.-Y.; Yuan, K.; Yang, W.; Zhong, D.-C.; Lu, T.-B. A template co-pyrolysis strategy towards the increase of amino/imino content within g-C_3N_4 for efficient CO_2 photoreduction. *Chem. Eng. J.* **2022**, 140630. [CrossRef]
199. Tang, Z.; Wang, C.; He, W.; Wei, Y.; Zhao, Z.; Liu, J. The Z-scheme g-C_3N_4/3DOM-WO_3 photocatalysts with enhanced activity for CO_2 photoreduction into CO. *Chin. Chem. Lett.* **2022**, *33*, 939–942. [CrossRef]
200. Sahoo, R.C.; Lu, H.; Garg, D.; Yin, Z.; Matte, H.R. Bandgap engineered g-C_3N_4 and its graphene composites for stable photoreduction of CO_2 to methanol. *Carbon* **2022**, *192*, 101–108. [CrossRef]
201. Madi, M.; Tahir, M. Highly stable $LaCoO_3$ perovskite supported g-C_3N_4 nanotextures with proficient charges migration for visible light CO_2 photoreduction to CO and CH_4. *Mater. Sci. Semicond. Process.* **2022**, *142*, 106517. [CrossRef]
202. Liu, T.; Hao, L.; Bai, L.; Liu, J.; Zhang, Y.; Tian, N.; Huang, H. Z-scheme junction Bi_2O_2 $(NO_3)(OH)$/g-C_3N_4 for promoting CO_2 photoreduction. *Chem. Eng. J.* **2022**, *429*, 132268. [CrossRef]
203. Li, Y.; Yin, Q.; Zeng, Y.; Liu, Z. Hollow spherical biomass derived-carbon dotted with SnS_2/g-C_3N_4 Z-scheme heterojunction for efficient CO_2 photoreduction into CO. *Chem. Eng. J.* **2022**, *438*, 135652. [CrossRef]
204. Li, X.; Li, S.; Xu, J.; Wang, L.; Liang, K.; Zhang, H.; Yu, X.; Liu, Z. Synergy of nitrogen vacancies and nanodiamond decoration in g-C_3N_4 for boosting CO_2 photoreduction. *Appl. Surf. Sci.* **2022**, *600*, 154199. [CrossRef]
205. Li, L.; Ma, D.; Xu, Q.; Huang, S. Constructing hierarchical $ZnIn_2S_4$/g-C_3N_4 S-scheme heterojunction for boosted CO_2 photoreduction performance. *Chem. Eng. J.* **2022**, *437*, 135153. [CrossRef]
206. He, J.; Wang, X.; Jin, S.; Liu, Z.-Q.; Zhu, M. 2D metal-free heterostructure of covalent triazine framework/g-C_3N_4 for enhanced photocatalytic CO_2 reduction with high selectivity. *Chin. J. Catal.* **2022**, *43*, 1306–1315. [CrossRef]
207. Zhu, X.; Deng, H.; Cheng, G. Facile construction of g-C_3N_4-$W_{18}O_{49}$ heterojunction with improved charge transfer for solar-driven CO_2 photoreduction. *Inorg. Chem. Commun.* **2021**, *132*, 108814. [CrossRef]
208. Yin, S.; Sun, L.; Zhou, Y.; Li, X.; Li, J.; Song, X.; Huo, P.; Wang, H.; Yan, Y. Enhanced electron–hole separation in SnS_2/Au/g-C_3N_4 embedded structure for efficient CO_2 photoreduction. *Chem. Eng. J.* **2021**, *406*, 126776. [CrossRef]
209. Xu, Y.; Jin, X.; Ge, T.; Xie, H.; Sun, R.; Su, F.; Li, X.; Ye, L. Realizing efficient CO_2 photoreduction in Bi_3O_4Cl: Constructing van der Waals heterostructure with g-C_3N_4. *Chem. Eng. J.* **2021**, *409*, 128178. [CrossRef]
210. She, S.; Zhang, X.; Wu, X.; Li, J.; Zhang, G. The fabrication of two-dimensional g-C_3N_4/$NaBiO_3$· $2H_2O$ heterojunction for improved photocatalytic CO_2 reduction: DFT study and mechanism unveiling. *J. Colloid Interface Sci.* **2021**, *604*, 122–130. [CrossRef]
211. Qin, Y.; Dong, G.; Zhang, L.; Li, G.; An, T. Highly efficient and selective photoreduction of CO_2 to CO with nanosheet g-C_3N_4 as compared with its bulk counterpart. *Environ. Res.* **2021**, *195*, 110880. [CrossRef] [PubMed]
212. Mkhalid, I.A.; Mohamed, R.M.; Ismail, A.A.; Alhaddad, M. Z-scheme g-C_3N_4 nanosheet photocatalyst decorated with mesoporous CdS for the photoreduction of carbon dioxide. *Ceram. Int.* **2021**, *47*, 17210–17219. [CrossRef]
213. Li, X.; Jiang, H.; Ma, C.; Zhu, Z.; Song, X.; Wang, H.; Huo, P.; Li, X. Local surface plasma resonance effect enhanced Z-scheme ZnO/Au/g-C_3N_4 film photocatalyst for reduction of CO_2 to CO. *Appl. Catal. B Environ.* **2021**, *283*, 119638. [CrossRef]

214. Li, X.; Guan, J.; Jiang, H.; Song, X.; Huo, P.; Wang, H. rGO modified R-CeO_2/g-C_3N_4 multi-interface contact S-scheme photocatalyst for efficient CO_2 photoreduction. *Appl. Surf. Sci.* **2021**, *563*, 150042. [CrossRef]
215. Chen, C.; Jin, J.; Chen, S.; Wang, T.; Xiao, J.; Peng, T. In-situ growth of ultrafine ZnO on g-C_3N_4 layer for highly active and selective CO_2 photoreduction to CH_4 under visible light. *Mater. Res. Bull.* **2021**, *137*, 111177. [CrossRef]
216. Wang, S.; Zhan, J.; Chen, K.; Ali, A.; Zeng, L.; Zhao, H.; Hu, W.; Zhu, L.; Xu, X. Potassium-doped g-C_3N_4 achieving efficient visible-light-driven CO_2 reduction. *ACS Sustain. Chem. Eng.* **2020**, *8*, 8214–8222. [CrossRef]
217. Vu, N.-N.; Kaliaguine, S.; Do, T.-O. Synthesis of the g-C_3N_4/CdS nanocomposite with a chemically bonded interface for enhanced sunlight-driven CO_2 photoreduction. *ACS Appl. Energy Mater.* **2020**, *3*, 6422–6433. [CrossRef]
218. Ma, W.; Wang, N.; Guo, Y.; Yang, L.; Lv, M.; Tang, X.; Li, S. Enhanced photoreduction CO_2 activity on g-C_3N_4: By synergistic effect of nitrogen defective-enriched and porous structure, and mechanism insights. *Chem. Eng. J.* **2020**, *388*, 124288. [CrossRef]
219. Guo, L.; You, Y.; Huang, H.; Tian, N.; Ma, T.; Zhang, Y. Z-scheme g-C_3N_4/Bi_2O_2 [BO_2 (OH)] heterojunction for enhanced photocatalytic CO_2 reduction. *J. Colloid Interface Sci.* **2020**, *568*, 139–147. [CrossRef]
220. Guo, H.; Ding, J.; Wan, S.; Wang, Y.; Zhong, Q. Highly efficient CH_3OH production over $Zn_{0.2}Cd_{0.8}S$ decorated g-C_3N_4 heterostructures for the photoreduction of CO_2. *Appl. Surf. Sci.* **2020**, *528*, 146943. [CrossRef]
221. Khan, I.; Yuan, A.; Khan, S.; Khan, A.; Khan, S.; Shah, S.A.; Luo, M.; Yaseen, W.; Shen, X.; Yaseen, M. Graphitic carbon nitride composites with gold and ZIF-67 nanoparticles as visible-light-promoted catalysts for CO_2 conversion and bisphenol A degradation. *ACS Appl. Nano Mater.* **2022**, *5*, 13404–13416. [CrossRef]
222. Dao, X.-Y.; Xie, X.-F.; Guo, J.-H.; Zhang, X.-Y.; Kang, Y.-S.; Sun, W.-Y. Boosting photocatalytic CO_2 reduction efficiency by heterostructures of NH_2-MIL-101 (Fe)/g-C_3N_4. *ACS Appl. Energy Mater.* **2020**, *3*, 3946–3954. [CrossRef]
223. Nemiwal, M.; Zhang, T.C.; Kumar, D. Recent progress in g-C_3N_4, TiO_2 and ZnO based photocatalysts for dye degradation: Strategies to improve photocatalytic activity. *Sci. Total Environ.* **2021**, *767*, 144896. [CrossRef] [PubMed]
224. Duan, Y.; Deng, L.; Shi, Z.; Liu, X.; Zeng, H.; Zhang, H.; Crittenden, J. Efficient sulfadiazine degradation via in-situ epitaxial grow of graphitic carbon nitride (g-C_3N_4) on carbon dots heterostructures under visible light irradiation: Synthesis, mechanisms and toxicity evaluation. *J. Colloid Interface Sci.* **2020**, *561*, 696–707. [CrossRef] [PubMed]
225. Zhao, Y.; Shi, H.; Yang, D.; Fan, J.; Hu, X.; Liu, E. Fabrication of a Sb_2MoO_6/g-C_3N_4 photocatalyst for enhanced RhB degradation and H_2 generation. *J. Phys. Chem. C* **2020**, *124*, 13771–13778. [CrossRef]
226. Hayat, A.; Sohail, M.; Ali Shah Syed, J.; Al-Sehemi, A.G.; Mohammed, M.H.; Al-Ghamdi, A.A.; Taha, T.; Salem AlSalem, H.; Alenad, A.M.; Amin, M.A. Recent advancement of the current aspects of g-C_3N_4 for its photocatalytic applications in sustainable energy system. *Chem. Rec.* **2022**, *22*, e202100310. [CrossRef] [PubMed]
227. Li, J.; Qi, Y.; Mei, Y.; Ma, S.; Li, Q.; Xin, B.; Yao, T.; Wu, J. Construction of phosphorus-doped carbon nitride/phosphorus and sulfur co-doped carbon nitride isotype heterojunction and their enhanced photoactivity. *J. Colloid Interface Sci.* **2020**, *566*, 495–504. [CrossRef]
228. Zhang, B.; Li, X.; Zhao, Y.; Song, H.; Wang, H. Facile synthesis of oxygen doped mesoporous graphitic carbon nitride with high photocatalytic degradation efficiency under simulated solar irradiation. *Colloids Surf. A Physicochem. Eng. Asp.* **2019**, *580*, 123736. [CrossRef]
229. Jiang, L.; Yuan, X.; Zeng, G.; Liang, J.; Wu, Z.; Wang, H.; Zhang, J.; Xiong, T.; Li, H. A facile band alignment of polymeric carbon nitride isotype heterojunctions for enhanced photocatalytic tetracycline degradation. *Environ. Sci. Nano* **2018**, *5*, 2604–2617. [CrossRef]
230. Chen, M.; Jia, Y.; Li, H.; Wu, Z.; Huang, T.; Zhang, H. Enhanced pyrocatalysis of the pyroelectric $BiFeO_3$/g-C_3N_4 heterostructure for dye decomposition driven by cold-hot temperature alternation. *J. Adv. Ceram.* **2021**, *10*, 338–346. [CrossRef]
231. Zhang, H.; Guo, L.-H.; Zhao, L.; Wan, B.; Yang, Y. Switching oxygen reduction pathway by exfoliating graphitic carbon nitride for enhanced photocatalytic phenol degradation. *J. Phys. Chem. Lett.* **2015**, *6*, 958–963. [CrossRef] [PubMed]
232. Li, X.; Yu, J.; Jaroniec, M. Hierarchical photocatalysts. *Chem. Soc. Rev.* **2016**, *45*, 2603–2636. [CrossRef] [PubMed]
233. Du, X.; Bai, X.; Xu, L.; Yang, L.; Jin, P. Visible-light activation of persulfate by TiO_2/g-C_3N_4 photocatalyst toward efficient degradation of micropollutants. *Chem. Eng. J.* **2020**, *384*, 123245. [CrossRef]
234. Zhou, W.-J.; Ma, L.-X.; Li, L.-Y.; Zha, M.; Li, B.-L.; Wu, B.; Hu, C.-J. Synthesis of a 3D Cu (II) MOF and its heterostructual g-C_3N_4 composite showing improved visible-light-driven photodegradation of organic dyes. *J. Solid State Chem.* **2022**, *315*, 123520. [CrossRef]
235. Shekardasht, M.B.; Givianrad, M.H.; Gharbani, P.; Mirjafary, Z.; Mehrizad, A. Preparation of a novel Z-scheme g-C_3N_4/RGO/$Bi_2Fe_4O_9$ nanophotocatalyst for degradation of Congo Red dye under visible light. *Diam. Relat. Mater.* **2020**, *109*, 108008. [CrossRef]
236. Liu, Y.; Shen, Z.; Song, J.; Qi, H.; Yin, C.; Zou, X.; Xia, Q.; Cui, L.; Li, X.; Wang, Y. Honeycomb-like g-C_3N_4/CeO_2-x nanosheets obtained via one step hydrothermal-roasting for efficient and stable Cr (VI) photo-reduction. *Chin. Chem. Lett.* **2020**, *31*, 2747–2751. [CrossRef]
237. Prabavathi, S.L.; Saravanakumar, K.; Park, C.M.; Muthuraj, V. Photocatalytic degradation of levofloxacin by a novel Sm_6WO_{12}/g-C_3N_4 heterojunction: Performance, mechanism and degradation pathways. *Sep. Purif. Technol.* **2021**, *257*, 117985. [CrossRef]
238. Deng, Y.; Liu, J.; Huang, Y.; Ma, M.; Liu, K.; Dou, X.; Wang, Z.; Qu, S.; Wang, Z. Engineering the photocatalytic behaviors of g/C_3N_4-based metal-free materials for degradation of a representative antibiotic. *Adv. Funct. Mater.* **2020**, *30*, 2002353. [CrossRef]

239. Paul, D.R.; Gautam, S.; Panchal, P.; Nehra, S.P.; Choudhary, P.; Sharma, A. ZnO-modified g-C_3N_4: A potential photocatalyst for environmental application. *ACS Omega* **2020**, *5*, 3828–3838. [CrossRef]
240. Wu, L.; Chen, Y.; Li, Y.; Meng, Q.; Duan, T. Functionally integrated g-C_3N_4@ wood-derived carbon with an orderly interconnected porous structure. *Appl. Surf. Sci.* **2021**, *540*, 148440. [CrossRef]
241. Yassin, J.M.; Taddesse, A.M.; Sánchez-Sánchez, M. Sustainable synthesis of semicrystalline Zr-BDC MOF and heterostructural Ag_3PO_4/Zr-BDC/g-C_3N_4 composite for photocatalytic dye degradation. *Catal. Today* **2022**, *390*, 162–175. [CrossRef]
242. Hasija, V.; Raizada, P.; Sudhaik, A.; Singh, P.; Thakur, V.K.; Khan, A.A.P. Fabrication of Ag/AgI/WO_3 heterojunction anchored P and S co-doped graphitic carbon nitride as a dual Z scheme photocatalyst for efficient dye degradation. *Solid State Sci.* **2020**, *100*, 106095. [CrossRef]
243. Feng, Z.; Zeng, L.; Zhang, Q.; Ge, S.; Zhao, X.; Lin, H.; He, Y. In situ preparation of g-C_3N_4/$Bi_4O_5I_2$ complex and its elevated photoactivity in Methyl Orange degradation under visible light. *J. Environ. Sci.* **2020**, *87*, 149–162. [CrossRef] [PubMed]
244. Zheng, C.-W.; Niu, H.-Y.; Liang, C.; Niu, C.-G.; Zhao, X.-F.; Zhang, L.; Li, J.-S.; Guo, H.; Liu, H.-Y.; Liang, S. A study on advanced oxidation mechanism of $MnCo_2O_4$/g-C3N4 degradation of nitrobenzene: Sacrificial oxidation and radical oxidation. *Chem. Eng. J.* **2021**, *403*, 126400. [CrossRef]
245. Yu, X.; Zhang, X.; Zhao, J.; Xu, L.; Yan, J. Flower-like shaped $Bi_{12}TiO_{20}$/g-C_3N_4 heterojunction for effective elimination of organic pollutants: Preparation, characterization, and mechanism study. *Appl. Organomet. Chem.* **2020**, *34*, e5702. [CrossRef]
246. Feng, S.; Chen, T.; Liu, Z.; Shi, J.; Yue, X.; Li, Y. Z-scheme CdS/CQDs/g-C_3N_4 composites with visible-near-infrared light response for efficient photocatalytic organic pollutant degradation. *Sci. Total Environ.* **2020**, *704*, 135404. [CrossRef]
247. Liang, Q.; Liu, X.; Shao, B.; Tang, L.; Liu, Z.; Zhang, W.; Gong, S.; Liu, Y.; He, Q.; Wu, T. Construction of fish-scale tubular carbon nitride-based heterojunction with boosting charge separation in photocatalytic tetracycline degradation and H_2O_2 production. *Chem. Eng. J.* **2021**, *426*, 130831. [CrossRef]
248. Huang, Y.; Li, B.; Wu, F.; Yang, B. Fabrication of novel flower-like Co_3O_4/g-C_3N_4 heterojunction for tetracycline degradation under visible light irradiation. *Mater. Lett.* **2022**, *311*, 131538. [CrossRef]
249. Chen, W.; Huang, J.; He, Z.-C.; Ji, X.; Zhang, Y.-F.; Sun, H.-L.; Wang, K.; Su, Z.-W. Accelerated photocatalytic degradation of tetracycline hydrochloride over $CuAl_2O_4$/g-C_3N_4 pn heterojunctions under visible light irradiation. *Sep. Purif. Technol.* **2021**, *277*, 119461. [CrossRef]
250. Shi, Y.; Li, J.; Wan, D.; Huang, J.; Liu, Y. Peroxymonosulfate-enhanced photocatalysis by carbonyl-modified g-C_3N_4 for effective degradation of the tetracycline hydrochloride. *Sci. Total Environ.* **2020**, *749*, 142313. [CrossRef]
251. Luo, J.; Dai, Y.; Xu, X.; Liu, Y.; Yang, S.; He, H.; Sun, C.; Xian, Q. Green and efficient synthesis of Co-MOF-based/g-C_3N_4 composite catalysts to activate peroxymonosulfate for degradation of the antidepressant venlafaxine. *J. Colloid Interface Sci.* **2022**, *610*, 280–294. [CrossRef] [PubMed]